A Linear Stochastic Dynamical Model of ENSO. Part II: Analysis

C. J. THOMPSON AND D. S. BATTISTI

Joint Institute for the Study of the Atmosphere and Ocean, University of Washington, Seattle, Washington

(Manuscript received 27 July 1999, in final form 6 March 2000)

ABSTRACT

In this study the behavior of a linear, intermediate model of ENSO is examined under stochastic forcing. The model was developed in a companion paper (Part I) and is derived from the Zebiak–Cane ENSO model. Four variants of the model are used whose stabilities range from slightly damped to moderately damped. Each model is run as a simulation while being perturbed by noise that is uncorrelated (white) in space and time. The statistics of the model output show the moderately damped models to be more realistic than the slightly damped models. The moderately damped models have power spectra that are quantitatively quite similar to observations, and a seasonal pattern of variance that is qualitatively similar to observations. All models produce ENSOs that are phase locked to the annual cycle, and all display the ''spring barrier'' characteristic in their autocorrelation patterns, though in the models this ''barrier'' occurs during the summer and is less intense than in the observations (inclusion of nonlinear effects is shown to partially remedy this deficiency). The more realistic models also show a decadal variability in the lagged autocorrelation pattern that is qualitatively similar to observations.

Analysis of the models shows that the greatest part of the variability comes from perturbations that project onto the first singular vector, which then grow rapidly into the ENSO mode. Essentially, the model output represents many instances of the ENSO mode, with random phase and amplitude, stimulated by the noise through the optimal transient growth of the singular vectors.

The limit of predictability for each model is calculated and it is shown that the more realistic (moderately damped) models have worse potential predictability (9–15 months) than the deterministic chaotic models that have been studied widely in the literature. The predictability limits are strongly correlated with the stability of the models' ENSO mode—the more highly damped models having much shorter limits of predictability. A comparison of the two most realistic models shows that even though these models have similar statistics, they have very different predictability limits. The models have a strong seasonal dependence to their predictability limits.

The results of this study (with the companion paper) suggest that the linear, stable dynamical model of ENSO is indeed a plausible hypothesis for the observed ENSO. With very reasonable levels of stochastic forcing, the model produces realistic levels of variance, has a realistic spectrum, and qualitatively reproduces the observed seasonal pattern of variance, the autocorrelation pattern, and the ENSO-like decadal variability.

1. Introduction

For the past decade, the dominant view of the fundamental character of ENSO is as an essentially deterministic phenomenon where all the important physics can be found in the coupled ocean–atmospheric dynamics of the equatorial Pacific. In this view, ENSO variability arises because the system is dynamically unstable, and ENSO irregularity is a consequence of deterministic chaos. The dominance of this viewpoint has largely been due to the success of intermediate coupled models (ICMs), at explaining the basic physics of ENSO, and at achieving some skill in predicting El Niño events. This success started with the Zebiak and Cane model, hereafter the ZC model (Zebiak and Cane 1987), which was the first coupled model to produce the ENSO-like variability.

An alternate hypothesis that is now gaining favor is that ENSO variability and irregularity are instead caused by external stochastic forcing. This hypothesis, articulated by Penland and Sardeshmukh (1995), proposes that fluctuations in the ocean and atmosphere, external to the coupled system in the equatorial Pacific, are the source of stochastic forcing that drives ENSO. If this forcing is acting on an unstable system (i.e., a system with self-sustaining oscillations) then it is a source of the irregularity of ENSO. Alternatively, if this forcing is acting on a stable system, then it is the source of both the systems variability and its irregularity.

For the sake of discussion, the space of possible ENSO models can be divided into the following categories: 1) deterministic versus stochastic, 2) linear versus nonlinear, and 3) stable versus unstable. The nonlinear category can be further subdivided into (i)

Corresponding author address: David Battisti, JISAO, University of Washington, Box 354235, Seattle, WA 98195-4235.
E-mail: david@atmos.washington.edu

''slightly'' nonlinear, which is a system where the nonlinearity simply acts as a mechanism to limit growth through saturation, and (ii) ''highly'' nonlinear, a system that displays chaotic behavior (in addition to saturation). Determining into which of the viable categories the real ENSO system falls has important implications about the predictability limit of the system, and strongly affects the types of data collection strategies and data assimilation strategies that are optimal for initializing forecast models. Given that the observational record is short, at most 100 years, the best way to determine the nature of ENSO irregularity will probably be to construct a physically based model that reproduces the behavior of ENSO accurately enough to be convincing. More work still needs to be done toward this goal, but some of the stochastic models that have been built do provide some insight into the causes of ENSO irregularity, and their implications for predictability are discussed below.

- *Stochastic, linear, stable.* Penland and Sardeshmukh (1995) built an empirical linear, stable, Markov model of the Pacific and Indian Ocean SST and showed that the model produced ENSO-like behavior under stochastic forcing. This empirical model demonstrated the viability of a linear stable model and generated interest in the stochastic hypothesis for ENSO. The ICM that will be analyzed in this paper also falls into this category. If ENSO is found to fall into this category, it implies shorter predictability limits than that of a deterministic system. This category also implies that ENSO predictability is a function only of season, and not a function of the current phase of ENSO.
- *Stochastic, slightly nonlinear, stable, or unstable.* A series of experiments were run by Moore and Kleeman (1999) where an existing ICM of ENSO by Kleeman (1993) was run with a variety of parameter regimes (both stable and unstable) and in a variety of stochastic forcing regimes. Irregular ENSO events were produced in both the stable and unstable regimes, but it was concluded that the stable regime appeared more realistic. Chang et al. (1996) similarly took an ICM and drove it stochastically in both stable and unstable (but nonchaotic) regimes, showing that both cases produced ENSO-like statistics. As with the linear case, shorter predictability limits are implied by this category than for a deterministic system.
- *Stochastic, highly nonlinear, stable, or unstable.* The stable category is probably essentially the same as the slightly nonlinear case, since it is unlikely that the chaos would be significant. Of interest to a study in this category is the relative importance of the chaotic versus stochastic process in reducing predictability. The study by Jin et al. (1996) found that the chaotic windows in parameter space are extremely narrow. However, even if the equations of the system indicated that the system were in a chaotic parameter regime, it would be of little importance if the external noise dominates the loss of predictability (as the linear and slightly nonlinear cases indicate).

The model used throughout this paper was developed in Thompson and Battisti (2000), hereafter TB2000. It is a linearized version of the Battisti (1988) variant of the ZC model, which has been made asymptotically stable by some parameter changes. Four variations of the model parameters, called the four ''candidate'' models, will be examined. In three of the models, designated T.97, T.80, and T.60, two physically justified parameter changes are made. The first is a reduction in the western boundary reflection efficiency to observed values, and the second is an increase in the mechanical damping of the ocean dynamics. These two parameter changes have the effect of making the model asymptotically stable, while preserving much of the system's transient growth. The ''T'' in the model names stands for ''transient growth,'' and the numbers give the factor by which the ENSO mode decays per year. For example, the amplitude of the ENSO mode of T.80 decays by 0.80 per year. These three models were designed to have a range of stability between nearly neutral for T.97 to very stable for T.60. The fourth candidate model, called N.97, represents the ''nominal'' model: in this model the system is neutralized by decreasing the strength of the coupling between the ocean and atmosphere. The model approximately preserves the ratio between the transient growth and modal growth of ENSO that exists in the original unstable version of the model (see Chen et al. 1997 or Thompson 1998a). The models T.80 and T.60 employ parameter values that are most consistent with constraints imposed by theory and observation.

In this paper, the term the ''ENSO mode'' refers to the least stable Floquet mode of the system. The Floquet modes are a generalization of the eigenmodes for a linear system where the operator matrix is a periodic function of time. In this case the periodicity is due to the prescribed annual cycle in the background fields of SST, ocean currents, and surface winds. The Floquet modes are calculated from the eigenvectors and eigenvalues of the yearly propagator matrix, where the eigenvectors (called Floquet multipliers) give the growth rate and frequency of the mode. All of the candidate models have an ENSO mode that looks qualitatively similar to the observed ENSO cycle, has a period of 3–4 years, and evolves by the so-called delayed oscillator physics as described by Battisti (1988) and Battisti and Hirst (1989).

The values of the important parameters used in each of the candidate models are listed in Table 1, along with the period and growth rate of the ENSO mode produced by each model. Figure 1 shows the real and imaginary parts of the SST of T.80's ENSO mode, which represent the peak and transition phases of the models ENSO cycle. The ENSO modes of the other candidate models look quite similar in structure to T.80s and are not shown.

TABLE 1. Transient growth model characteristics. Parameter values and derived characteristics of the four candidate models. The bold entries are the nominal model values, taken from Battisti (1988). The coupling factor is the product of the drag coefficient, C_D, and the atmospheric heating constant, γ, normalized by the values of C_D and γ found in the Battisti (1988) model. The western boundary reflection coefficient (WBR) is the ratio of the returned Kelvin energy due to an incident gravest mode Rossby energy. The WBR is normalized by the fraction of energy (0.5) that is returned as a Kelvin signal in a perfectly efficient reflection of the gravest Rossby signal incident upon a meridional wall. The ocean damping rate is the prescribed Rayleigh damping time of the first vertical mode in the ocean. The last two rows show the growth rate and period of the leading Floquet mode of each model (i.e., that model's ENSO mode). The singular value is the maximum for any start month and period of optimization.

Model designation	N.97	T.97	T.80	T.60
Coupling factor ($\gamma \cdot C_D$)	0.75	**1.00**	**1.00**	**1.00**
Western boundary reflection (WBR)	**1.00**	0.8	0.7	0.7
Ocean damp (months)	**30**	10	8.7	6.5
ENSO growth per year	0.97	0.97	0.80	0.60
ENSO period (years)	2.89	3.42	3.85	4.32
Singular value (maximum)	6.3	10.3	9.6	8.9

In this study, each of the four candidate models will be run as simulations, perturbed stochastically by white noise. A number of statistical tests will be preformed on the output of these models and the results of each model will be compared to and contrasted with those obtained from the observations and from the other models. The statistics will show that output from the moderately damped models T.80 and T.60 is more consistent with observations than the output from the nearly neutral models. The T.80 and T.60 models have power spectra that are quantitatively similar to observations, and a seasonal pattern of variance that is qualitatively similar to observations. It will also be shown that the models reproduce the ''spring barrier'' characteristic of the autocorrelation pattern. In the models this ''barrier'' occurs during the summer and is less intense than in the observations; nonlinearity will be shown to account for much of these discrepancies in the T.80 model. Analysis of the models will show that the greatest part of the variability comes from perturbations that project onto the first singular vector, which then grow rapidly into the ENSO mode. Essentially, the model output represents many instances of the ENSO mode, with random phase and amplitude, stimulated by the noise through the optimal transient growth of the singular vectors.

The limit of predictability for each model is evaluated in section 4. It is shown that the more realistic (moderately damped) models have worse potential predictability (9–15 months) than deterministic chaotic models. It is also shown that the predictability limits are strongly correlated with the growth rate of the ENSO mode in the model, the more highly damped models having much shorter limits of predictability. A comparison of T.80 and T.60 also shows that even though the two models have similar statistics, they have very different predictability limits, with strong seasonal dependance.

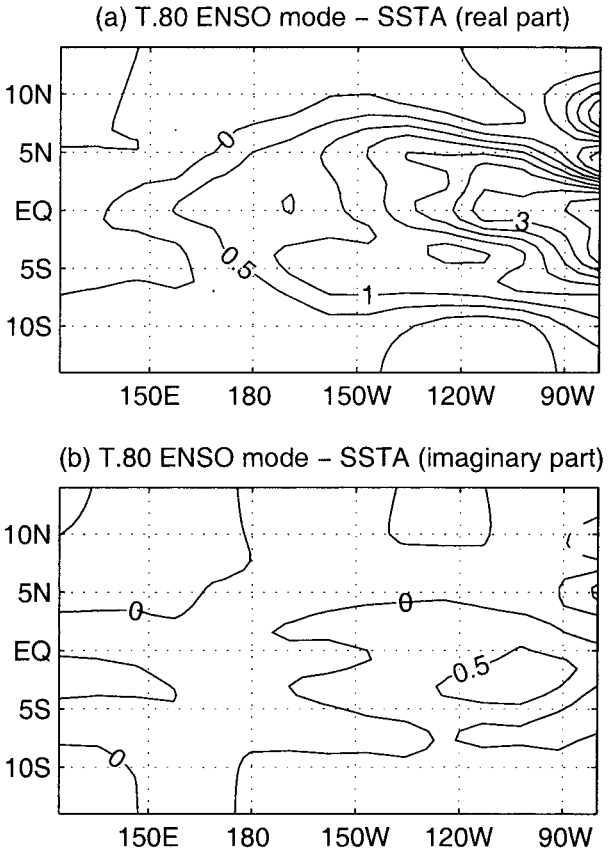

FIG. 1. Real and imaginary parts of T.80 ENSO mode. (a) The real part of the T.80 ENSO mode that corresponds to the mature phase of ENSO, and (b) the imaginary part that corresponds to the transition phase of ENSO.

The paper is divided into six sections. Section 2 explains the method used for the stochastic simulations and shows the results of the statistical tests. In section 3 the model statistics are explored in more depth and relationships between some of the statistical quantities are posited. Section 4 explores the predictability limits of ENSO implied by the models. Section 5 is a discussion about the paper's results and their implications about the stochastic ENSO hypothesis. Section 6 is the summary.

2. Stochastic simulations

The four candidate models developed in TB2000 will now be driven stochastically to examine whether they produce ENSO events with spatial structure and temporal statistics that are similar to those observed. The models will be driven through the addition of perturbations to the state variables at monthly intervals. Random perturbations were used for the stochastic forcing since the model, developed as a tool to calculate eigenvalues and singular values, cannot be externally forced in its present configuration. Mathematically, the state of the system is advanced 1 month using

TABLE 2. Noise forcing distributions. The standard deviations of the noise used to drive each of the candidate models. For the thermocline perturbations, which are not quite spatially uniform, the shape of the distribution can be found in Fig. 9. The thermocline numbers represent the maximum standard deviation found in Fig. 9.

Model	N.97	T.97	T.80	T.60
STA max std (degree)	0.20	0.10	0.24	0.31
Thermocline max std (meters)	1.5	1.2	2.8	3.9

$$\begin{bmatrix}\mathbf{r}\\ \mathbf{T}\end{bmatrix}_{n+1} = \mathbf{R}_m\begin{bmatrix}\mathbf{r}\\ \mathbf{T}\end{bmatrix}_n + \begin{bmatrix}\mathbf{r}\\ \mathbf{T}\end{bmatrix}_{\text{random}}, \quad (1)$$

where **r** is the vector describing the ocean discretization, **T** is the SSTA discretization, $\mathbf{R}_m$ is the linear propagator for the appropriate month of the year, and $[\mathbf{r}\ \mathbf{T}]_{\text{random}}$ is a random perturbation with some prescribed distribution.

The SSTA and ocean dynamics are perturbed in separate experiments. It is hypothesized from the results of Thompson (1998a) that the perturbations on the sea surface temperature anomaly (SSTA) or on the ocean dynamics will produce qualitatively similar responses in the model, since the optimal initial conditions (first singular vectors) of either field produce a similar response. This hypothesis depends on the assumption that most of the variance in the model output will be the result of exciting the first singular vector—an assumption that will be verified in section 3.

Each of the four candidate models was run through a 1000-yr simulation, where once a month, either the SSTA or ocean dynamics was perturbed through the addition of a randomly generated field with a constant normal distribution. Therefore forcing is both spacially and temporally uncorrelated. (See appendix D of Thompson 1998b, for details of the discretization scheme.) Remember that in these models the winds are always in equilibrium with, and determined by, the SSTA, and thus are also perturbed. Likewise, the ocean perturbation affects both the thermocline and currents.

For each model, the forcing amplitude was scaled so that the average variance of the Niño-3 index (SSTA average in the area 5°N–5°S, and 150°–90°W) from the simulation would match the average Niño-3 variance of the Comprehensive Ocean–Atmosphere Data Set (COADS) data. For all models, the random number generator was started with the same seed, and so the random perturbations for each simulation are identical in shape at each time step, but have different amplitudes as determined by each model's sensitivity. All runs were started with all fields initially set to zero.

a. SSTA–pertubed simulations

The first set of runs was made by perturbing the SSTA alone. The amplitude of the stochastic forcing is shown in Table 2. None of the models requires excessive forcing to produce ENSO events of realistic amplitude. The least sensitive of the models, T.60, requires noise with a maximum standard deviation of only 0.31°C to achieve the same average variance level as the observed Niño-3 index.

1) TIME SERIES

The time series of the Niño-3 index for the first 120 yr of the simulations are shown in Fig. 2, along with the 42-yr time series of COADS data. Even without any sophisticated tests, the increasing irregularity of the models from N.97 to T.60 is apparent. Note that all of the models, that start at rest, ''spin up'' fairly quickly, producing their first ENSO event within 15 yr. As might be expected because of their nearly neutral ENSO modes, both N.97 and T.97 display unrealistically long periods of regular ENSO events, while the more damped models, T.80 and T.60, show no such long-term oscillating regimes.

2) EOFS

Figure 3 shows the first two EOFs of SSTA from the simulation of the T.80 model along with the first two EOFs from the COADS data. The first two EOFs of N.97, T.97, and T.60 look quite similar to those of T.80 and are not shown. Table 3 shows the percent of variance explained by each of the first 3 EOFs for the models and the observations, from which it can be seen that the first EOF dominates the variability. The most significant EOF of the model data looks similar to the first EOF of the COADS data, except that the center of action in the models is more equatorially confined. In both the data and model output, this first EOF represents the shape of the ENSO cycle during its mature phase (e.g., at the peak of a warm or cold event.) The second EOF of the model output bears no obvious relationship to the second EOF of the observations, nor to any subsequent observational EOF (not shown.) The second EOF of the model seems roughly to represents the transition phase of the ENSO mode as suggested by comparison with the imaginary phase of the ENSO mode in Fig. 1.

3) POWER SPECTRA

Figure 4 shows the power spectra of the Niño-3 index for the four models (thick lines), and observations (thin lines). The spectral analysis of the four models was performed on the 1000-yr simulations using a covariance power spectrum method with a 40-yr window. As might be expected from an inspection of the time series in Fig. 2, the N.97 and T.97 show a strong peak near the period of their respective ENSO modes. Models N.97 and T.97 also show a distinct secondary peak (local maximum) at 1.5 and 1.3 yr, respectively. This secondary peak is part of the ENSO mode and will be discussed in section 3. Table 4 lists the periods of the peak fre-

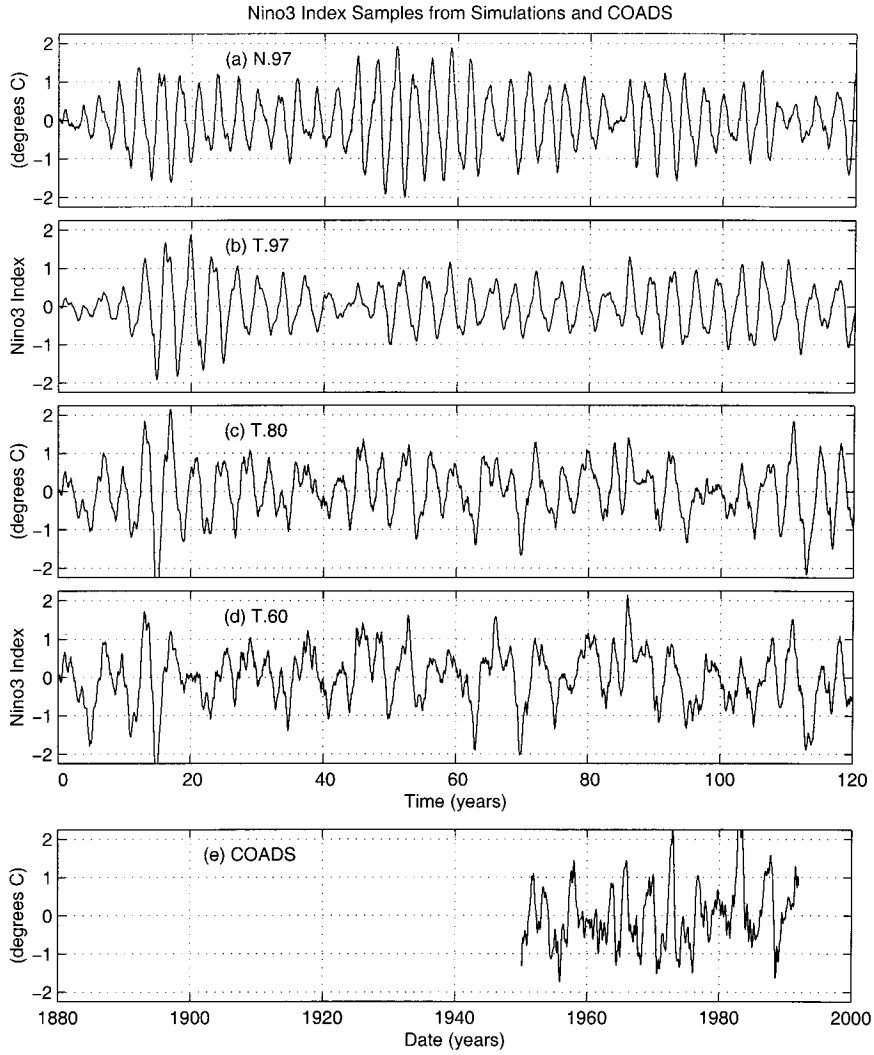

FIG. 2. Niño-3 index of first 120 yr of simulations plus COADS. (a)–(d) The Niño-3 index of the first 120 yr of the SSTA forced N.97, T.97, T.80, and T.60 simulations, respectively. (e) The Niño-3 index of the 42 yr of COADS data.

quency, the secondary peak, and the ENSO mode, for each model.

The spectrum of model T.60 is quite different from T.97 and N.97. Instead of a single peak near its ENSO mode period, it has a broad plateau that stretches from about 3.4 to about 6.4 yr. This plateau straddles the ENSO period for T.60, which is 4.3 yr, but there is no peak at this point in the spectrum. The secondary peak at 1.3 yr is present in the T.60 spectrum, but is indistinct. The T.80 spectrum has a mixture of the characteristics of the broad spectrum of T.60 and the ''peakier'' spectra of T.97 and N.97. The highest peak is near its ENSO mode period of 3.85 yr, but the peak is much broader than the peaks of T.97 and N.97. The secondary local maximum is there also, but it too is not as distinctive as in T.97 and N.97.

Of the four candidate models, the T.80 spectrum most closely matches the COADS spectrum. For periods longer than about 2.5 yr, the T.80 spectrum is quite a close match to COADS. However, while the model simulations are long enough to resolve their spectra, the COADS dataset is quite short.[1] The window on the covariance power spectrum method was set to 40 yr, which means that the simulations are effectively the average of 25 instances of 40 yr of data, whereas the 42 yr of COADS data is just a single instance. To estimate the range of the spectra that might be expected from a 42-yr dataset, the 1000-yr simulations were divided into 42-yr samples, and the spectrum for each sample was computed individually. The dashed lines in Fig. 4 show the envelope of the spectra for each model, where the

[1] While the extended COADS dataset could have been used to achieve greater degrees of freedom, the quality of the data increasingly suffers as the record is extended back beyond 1950.

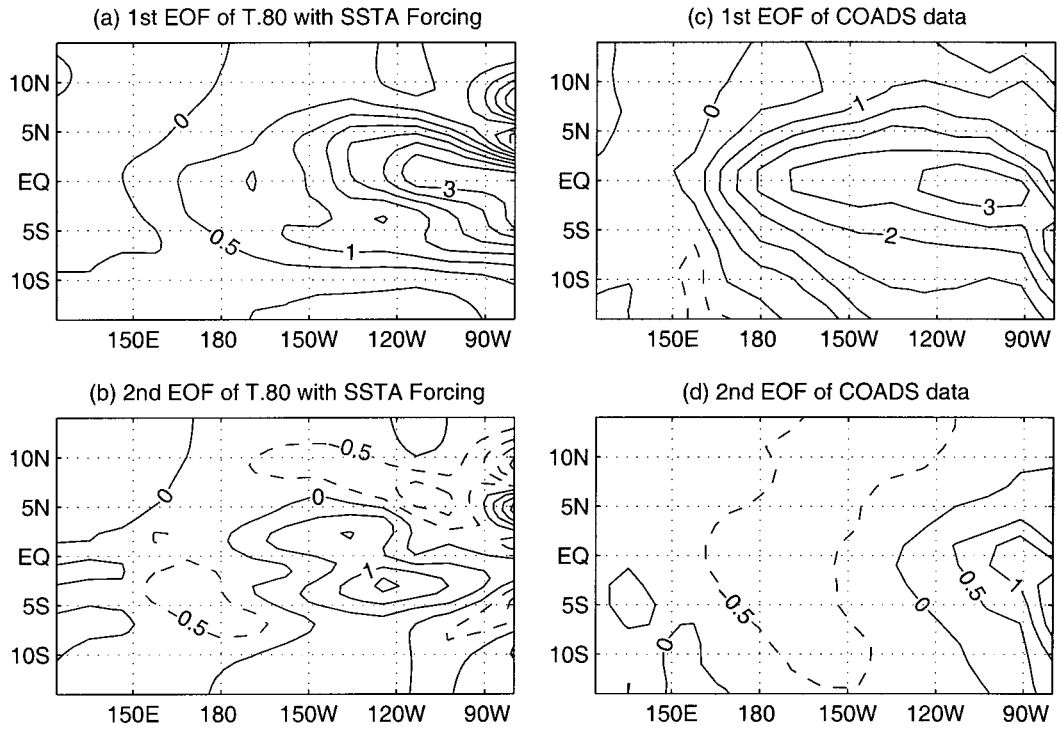

FIG. 3. First two EOFs of T.80 simulation and COADS. (a) The first EOF calculated from the T.80 simulation output, and (b) the second EOF of the same. The first EOF corresponds to the mature phase of ENSO and the second EOF corresponds to the transition phase. (c)–(d) The first and second EOFs of the COADS data.

envelope is defined as the range into which the middle 80% of the sample spectra fall. For the T.80 and T.60 models, the COADS spectrum is largely within the envelope for periods over 2 yr. The COADS spectrum falls outside the spectral envelopes for T.97 and N.97, except in very narrow ranges near the primary and secondary peaks.

From a comparison of the spectra, T.80 seems the most plausible of the models, with T.60 coming in a close second. However, none of the model spectra are very good at the higher frequencies. For periods of 1 yr or less, this discrepancy might be attributable to the long wavelength formulation of the models, or even to the presence of measurement error in the observation. But at a period of around 2 yr the models are particularly bad, and this seems likely due to a model deficiency. In particular, it may be exposing the limitations associated with a 1.5-layer approximation to a continuously stratified ocean (see, e.g., Y.-Q. Chen et al. 1995), or the neglect of nonlinear processes (see section 5f).

TABLE 3. Percent variance explained SSTA forcing. The percent variance explained for the first three EOFs of each of the model simulations and observations.

Model	N.97	T.97	T.80	T.60	COADS
1st EOF	69.5	86.0	65.0	54.6	55.1
2d EOF	3.6	4.3	3.3	2.8	11.5
3d EOF	1.4	1.6	1.7	1.7	6.0

4) SEASONAL PATTERN OF VARIANCE

The real ENSO system has a tendency to peak during the winter months, as can be inferred by the wintertime maximum in the standard deviation of the monthly mean SSTA in Niño-3. Figure 5 shows the monthly standard deviation of the Niño-3 index for each of the candidate models. As was hypothesized in TB2000, these models show greater variation during the winter months even though they are perturbed uniformly in time. Despite having different spectra, all of the models have a similar seasonal distribution of variance.

The COADS data appears in Fig. 5 for reference. While there is a qualitative similarity between observations and the model output, there are a number of quantitative differences. Both the simulations and the COADS data have their maxima around December, however, the variance in the observations falls rapidly, having its minimum in March, whereas the models' variance fall more gradually to bottom out in June. While models and observation have the same annually averaged variance (by design) the observations have a slightly larger seasonal change in variance than the models.

In order to test the robustness of the seasonal pattern of variance in the models, the 1000-yr simulations were again divided into 42-yr samples, and the range of these samples examined. This sensitivity experiment showed the seasonal pattern of variance to be well resolved even for a 42-yr sample. The sample range is not shown in

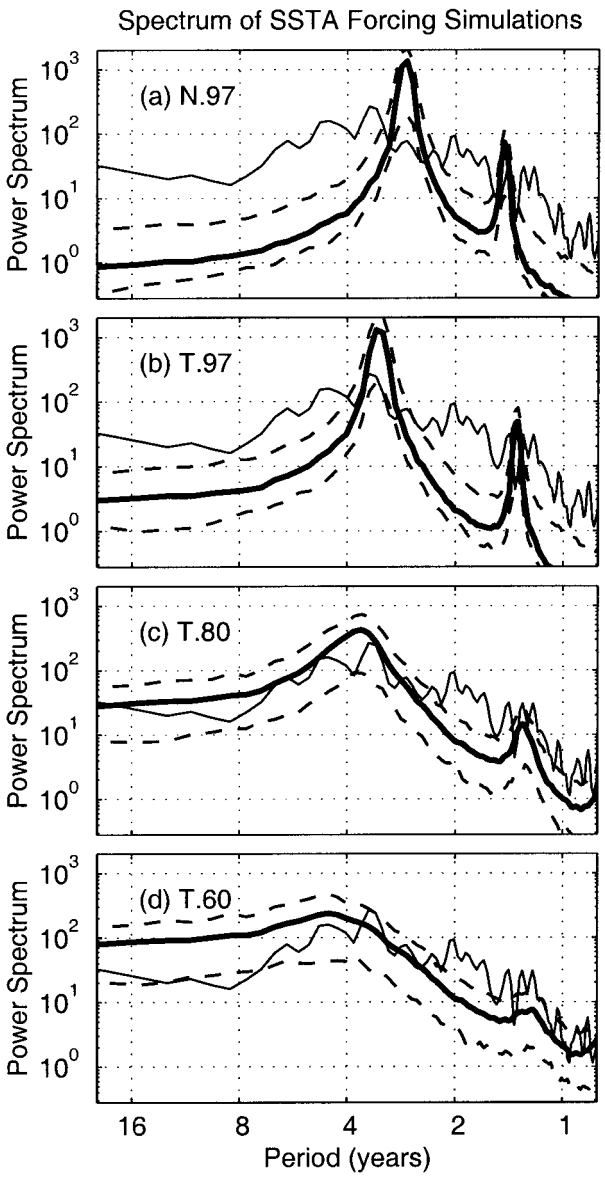

FIG. 4. Power spectra of candidate models. The thick lines in (a)–(d) show the spectrum of the Niño-3 index for the models N.97, T.97, T.80, and T.60, respectively. The pair of dashed lines in each give an estimate of the range that could be expected given a 42-yr sample of each model. This range was determined by dividing a 10 000-yr simulation into 42-yr samples—80% of the samples fall between the dashed lines. For comparison, the COADS spectrum is included in each (thin lines).

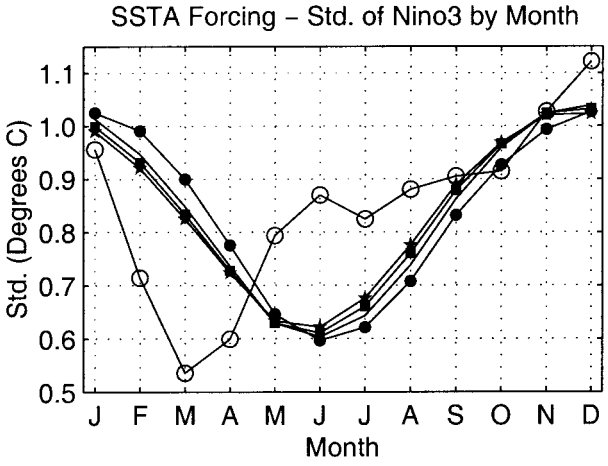

FIG. 5. Annual cycle of variance: the standard deviation of the Niño-3 index by month for the 1000-yr model simulations and the COADS data. The key is as follows: open circles are COADS data; solid circles are N.97; unmarked line is T.97; squares are T.80; stars are T.60.

Fig. 5, but for all models the range of standard deviation for any month is less than ± 0.05°C. The errors in the model seasonal patterns of variance most likely cannot be attributed to sampling error in the observations. Therefore, while the models do produce a seasonal pattern qualitatively similar to the observations, this pattern is about 30% too weak, and has its minimum 3 months late.

5) LAGGED AUTOCORRELATION

The autocorrelation of the Niño-3 index for each of the four candidate models and the COADS data is shown in Fig. 6. The autocorrelation for the COADS data shows the well-known spring barrier—a precipitous drop in persistence starting in the spring following the forecast start time (Walker and Bliss 1937). The N.97 and T.97 autocorrelation graphs also show a clear drop in persistence. However, for these models, the drop in persistence is less severe than in the observations, and occurs in the summer rather than the spring. The more highly damped models, T.80 and T.60 also show this ''summer barrier,'' but it is even less intense than T.97 and N.97.

TABLE 4. Power spectra peak values: SSTA forcing. The period of the peak frequency in the power spectrum (Fig. 4) for each model and the COADS data. Also included for each of the model simulations are the periods of the second local maxima. There is no obvious secondary peak in the COADS spectrum.

Model	N.97	T.97	T.80	T.60	COADS
Spectrum peak period (yr)	2.7	3.3	3.6	3.3 to 6.4	3.5
Spectrum 2d local max period (yr)	1.5	1.4	1.3	1.3	—
ENSO mode period (yr)	2.9	3.4	3.9	4.3	—

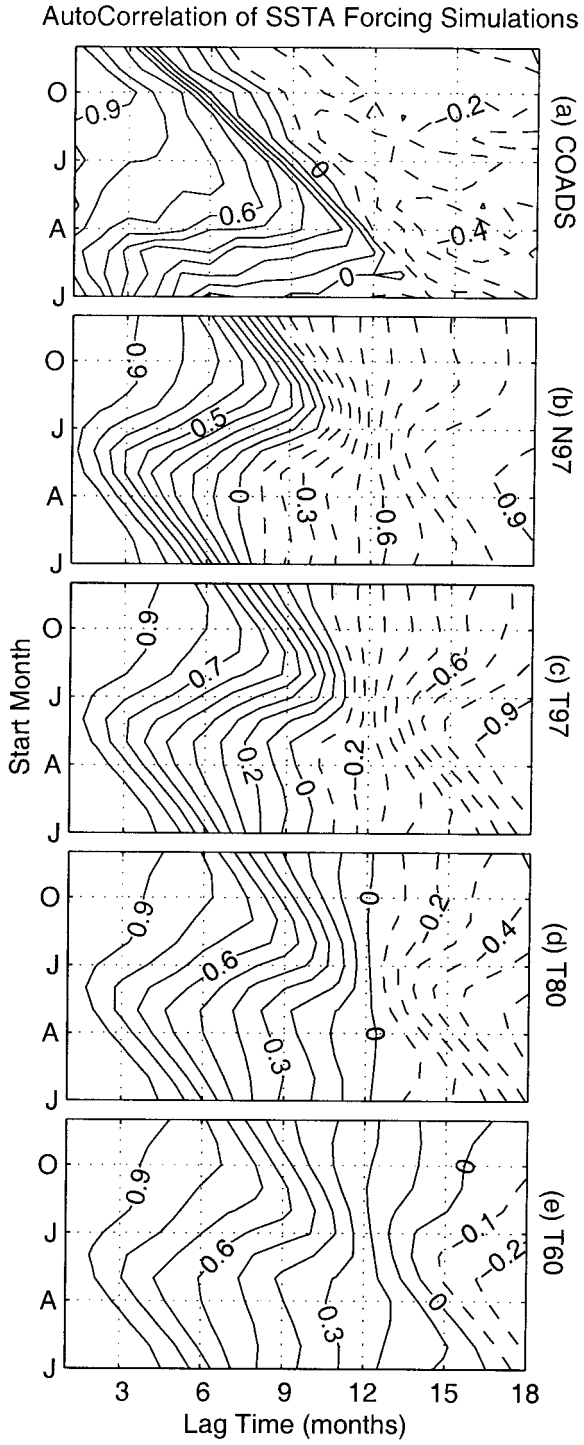

FIG. 6. Autolag correlation of simulation and observations. Autolag correlation starting at each month of the year out to lag times of 18 months. (a) The COADS data, while (b)–(e) are for the N.97, T.97, T.80, and T.60 models, respectively. Contour increment is 0.1 for all graphs.

6) DECADAL VARIABILITY IN LAGGED AUTOCORRELATION

A number of different researchers have noted an apparent decadal variation in the lagged autocorrelation pattern of ENSO (e.g., Balmaseda et al. 1995; Torrence and Webster 1998; Flügel and Chang 1999). Specifically, the spring barrier, which is quite pronounced between the mid-1940s and 1975, is very weak after 1975. Figures 7a and 7b show the lagged autocorrelation maps in the COADS data for the 15-yr periods before and after 1975, respectively. The earlier time period has a pronounced drop in the correlation for lag times that encroach into the first spring after the start month. After 1975, while there is still a tendency for correlation to drop during the spring, the correlation degrades in a more uniform manner.

Following Flügel and Chang (1999), autolog correlation maps were calculated over 15-yr periods for a 500-yr simulation of the T.80 model. These maps were examined to find adjacent 15-yr periods that show a marked change in the summer barrier found in the model. Figures 7c and 7d show an example from the simulation that makes just such a change. Figure 7c shows that lagged autocorrelation for years 337–352 of the T.80 simulation. In this period, the summer barrier is pronounced, that is, the correlation drops steeply for lag times that project into the first summer after the start month. (Note that in Figs. 7c and 7d, the ''start month'' axis has been shifted by three months to make comparisons with Figs. 7a and 7b easier.) This drop in correlation is not as steep as that for the 1960–75 COADS data, but is certainly more pronounced than the average summer barrier for this model, shown in Fig. 6d. Figure 7d shows the lagged autocorrelation for the subsequent 15-yr period, simulation years 352–367. In this time period the summer barrier is less pronounced than the average of Fig. 6d, but still retains a tendency for the correlation to drop during the summer.

In the 500 years of T.80 simulation that were examined, three transitions in the autocorrelation pattern were found with the same characteristics and magnitude as shown in Figs. 7c and 7d. The T.80 simulation seemingly has decadal variation in its autocorrelation analogous to the observed decadal variation. It is unclear if the decadal variation in the observations is caused by a decadal timescale mechanism, or if it is merely an artifact of the sample size being too short to resolve the statistic. For the model, however, there are no inherent decadal-scale processes. The decadal variability in the model is simply due to the random external forcing that is prescribed.

b. Ocean dynamics (thermocline) perturbed runs

A second set of 1000-yr simulations was run with stochastic perturbations made to the ocean dynamics rather than the SSTA. For these runs, the components

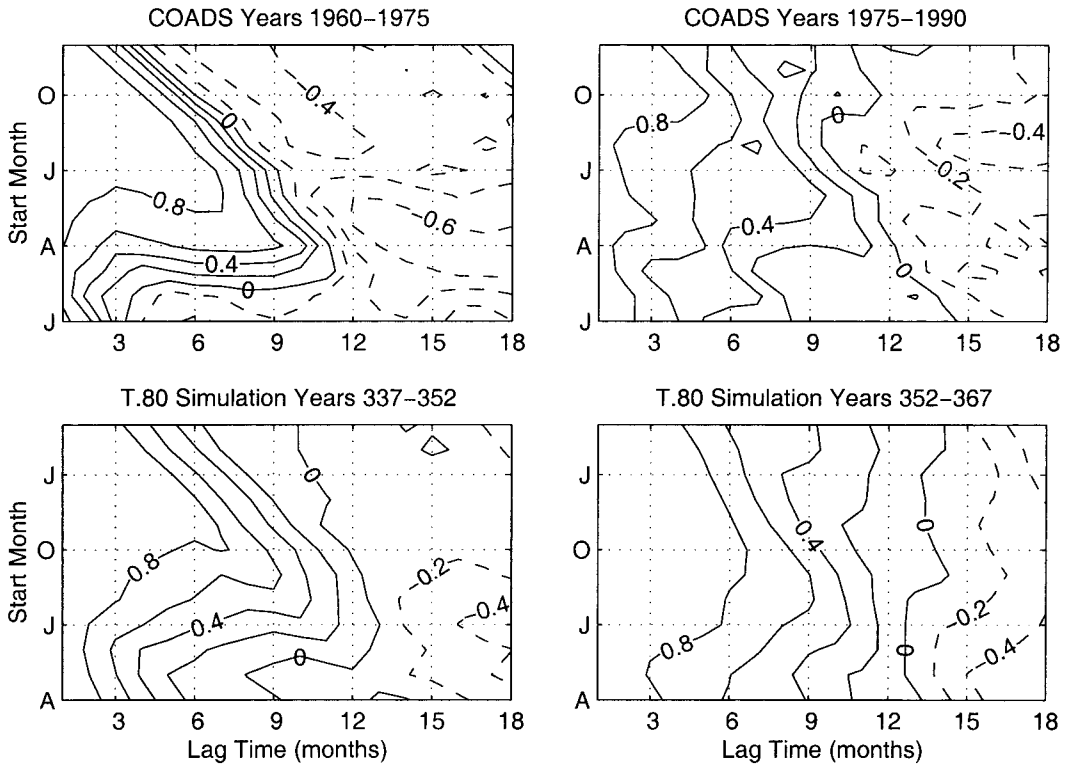

FIG. 7. Decadal variation in autolag correlation patterns. All four panels show the autolag correlation out to 18 months for a different 15-yr time period. (top) The COADS data, periods 1960–75 (left) and 1975–90 (right). (bottom) The T.80 simulation years 337–52 (left) and 352–67 (right). Contour increment is 0.1 for all graphs.

of the state variable **r** [see Eq. (1)] were perturbed once a month with a normal distribution, uncorrelated in space and time. Since the components of **r** are the amplitudes of the equatorial ocean modes (Kelvin and Rossby waves), the stochastic forcing on the thermocline is not uniformly distributed in space. Figure 8 shows how the normally distributed forcing of **r** maps to the thermocline. The maximum amplitude of the perturbation forcing required for each model to match the observed annually averaged variance of the monthly Niño-3 index is listed in Table 2.

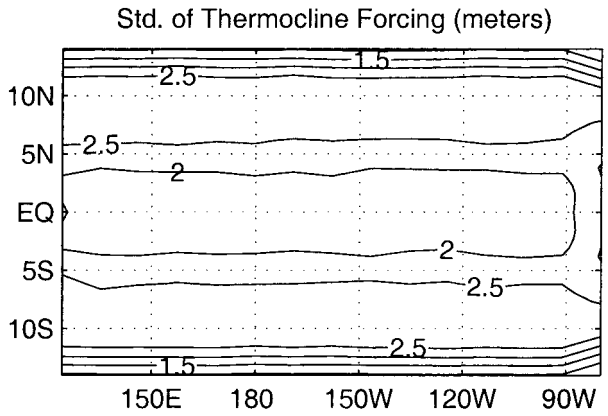

FIG. 8. Spatial distribution of thermocline perturbations. Spatial distribution of the standard deviation of thermocline used in ocean dynamics forced stochastic simulations. All four models have the same spatial distribution, but the magnitude varies. The distribution pictured is that of the T.80 model, the magnitude used on the other models is listed in Table 3. The contour interval is 0.5 m.

All the statistical tests that were run on the SSTA-forcing simulations were also run on the ocean dynamics forcing simulations (e.g., the EOFs, spectra, seasonal pattern of variance, and lagged autocorrelation). The results of these tests on the thermocline noise case, while slightly different quantitatively, were qualitatively the same as in the SSTA noise case (Figs. 2–7) and will not be shown.

3. Analysis of stochastic simulations

In this section, the reaction of the four candidate models to stochastic forcing will be explored in more depth. Figure 2 shows the Niño-3 index for each of the models over the first 120 yr of simulation. Each of the models shows some degree of irregularity—T.80 and T.60, in particular, show variability similar to the COADS Niño-3 index. Looking only at the Niño-3 index, however, does not provide a sense of how the imposed perturbations cause the irregularity. Is a warm event caused by a single perturbation that just happens to be at the right time of the year and projects strongly onto the first

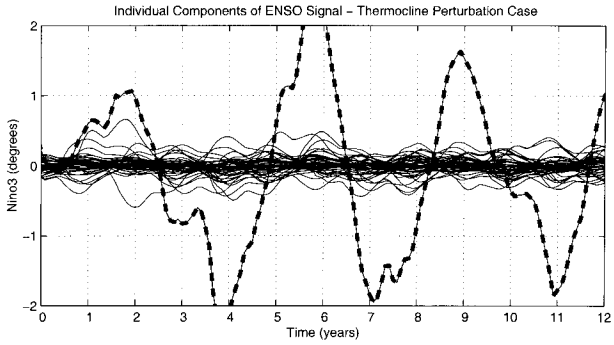

FIG. 9. Sum of individual perturbation for 12 yr of T.80 simulation. The thick dashed line shows the Niño-3 index for a 12-yr sample of the T.80, ocean dynamics forced simulation. The thin lines show the time evolution of each of the individual monthly perturbations. If the thin lines are added together, they sum up to the thick dashed line, which is the actual response of the model.

singular vector? Or is the growth more likely to be the result of many perturbations added together? How important is the first singular vector pattern to the overall response of the model?

a. Cause of irregularity

Since these simulations are linear, the exact contribution of each noise perturbation can be calculated: the amplitude of Niño-3 at any point in time is equal to the sum of the contributions of all the perturbations that came before it. Mathematically,

$$\begin{bmatrix}\mathbf{r}\\ \mathbf{T}\end{bmatrix}_n = \sum_{m=0}^{n} \mathbf{R}(t_n, t_m)\begin{bmatrix}\mathbf{r}\\ \mathbf{T}\end{bmatrix}_{\text{random},m}, \qquad (2)$$

where $\mathbf{R}(t_n, t_m)$ is the linear propagator from month m to month n, and $[\mathbf{r}\ \mathbf{T}]_{\text{random},m}$ is the random perturbation at month m. This equation shows that the signal at any time is affected by every perturbation that precedes it, but does not indicate whether a small number of perturbations (or a single perturbation) might dominate the solution.

Figure 9 shows 12 yr of output from the T.80 model driven by thermocline perturbations. The thick dotted line shows the total Niño-3 index, and the solid lines show the evolution of Niño-3 for each of the monthly perturbations, propagated forward individually. When all of the solid lines are added together, the result is the dashed line. From Fig. 9 it can clearly be seen that any given ENSO event is the result a large number of the preceding perturbations. For example, the warm event occurring in year 6 has a magnitude of over 2 degrees, but no single perturbation contributes more than 0.5 degrees to the total.

Figure 9 demonstrates that ENSO events may be the result of the sum of a large number of unrelated small random perturbations. This result assumes that the random forcing has distribution that is relatively uniform in time. If the forcing is itself structured in time (i.e., the Madden–Julian oscillation, Madden and Julian 1972) *and* it projects strongly onto the first singular vector, then a small number of perturbations may be disproportionately responsible for individual warm or cold events. Whether ENSO events are a result of random or organized (uncoupled) forcing has implications for the limit of predictability of ENSO, as well as the optimal method of data assimilation for forecasting. For instance, if ENSO events are usually caused by a single, distinct, precursor event, the best method of forecasting might be to resolve this event (i.e., look for the principal singular vector), whereas if ENSO events are caused by the sum of small-amplitude noise forcing over several years, then resolving the phase and amplitude of the ENSO mode (i.e., the principal eigenvector) might well be the optimal forecasting strategy. The predictability implications of these models are discussed in section 4, but the data assimilation question is beyond the scope of this paper.

b. Dominance of the first two singular vectors

A second question of interest is how important the principal singular vector (or optimal structure) is to the stochastically forced models. To explore this question, a set of simple experiments were performed. All the simulations from section 2 were run again, but this time only the portion of the perturbations that projects onto the first singular vector were used to perturb the model. The seeds in the random number generators were not changed, so the singular vector projected run could be compared directly to the original simulations. This experiment was then repeated, but projecting the perturbations onto the first two singular vectors, then the first three singular vectors, and so on. The noise was projected onto a single pattern, the pattern that gives optimal growth in the SST over nine months, starting in May (see Fig. 4 from TB2000). Using this optimal structure—instead of recalculating the pattern for each month—is justified because the shapes of the optimals for different start months and time periods are very similar (TB2000).

Two different measures were used to gauge the importance of a given set of singular vectors to the model output: (i) the correlation coefficient between the original Niño-3 time series and time series with the modified forcing, and (ii) the percent variance defined by:

$$\text{PVI} = \text{Percent Variance Induced} \equiv 100 \cdot (V_O - V_E)/V_O, \qquad (3)$$

where V_O is the variance of the original time series, and V_E is the variance of the error time series. Here V_E is defined as the difference between the original Niño-3 index and the Niño-3 index with the truncated noise forcing. The PVI is *not* the same as the ''percent variance explained'' commonly used with EOFs, since the set of singular vectors do not remain orthogonal as they

TABLE 5. Correlation with noise projected onto singular vectors. Correlation of the Niño-3 index from a model forced with random noise with the Niño-3 index from a simulation where the (identical) noise forcing is first projected onto a subset of the singular vectors before it is used to force the same coupled model. The row labeled ''subsequent'' indicates the maximum increase in the correlation achieved by the addition of any individual subsequent singular vector beyond the third.

Singular vectors	N.97	T.97	T.80	T.60
1st	0.80	0.80	0.82	0.82
1st and 2d	0.87	0.87	0.88	0.88
1st, 2d, and 3d	0.87	0.90	0.90	0.90
Subsequent	<0.01	<0.01	<0.01	<0.01

TABLE 6. Percent variance achieved with noise projected onto singular vectors. The percent variance achieved [as defined by Eq. (3)] in the Niño-3 index of a stochastic simulation where the random noise is projected onto a subset of the singular vectors before it is used to force the coupled model, as compared with the Niño-3 index of a simulation forcing by the identical noise that has not been truncated. The row labeled subsequent indicates the maximum increase in the percent variance achieved by the addition of any individual subsequent singular vector beyond the third.

Singular vectors	N.97	T.97	T.80	T.60
1st	64	64	67	67
1st and 2d	75	76	77	77
1st, 2d, and 3d	75	80	80	81
Subsequent	<4	<2	<2	<2

evolve with time. However, the PVI does give a normalized gauge of the importance of the set of singular vectors used. The smaller the variance of the error relative to the total variance, the closer the PVI will get to 100%. Longer simulations (10 000 yr) were required to resolve the PVI to within a certainty of 2 percent.

Table 5 shows the results of the correlation tests for the models when driven by SSTA noise. All models show a correlation of 0.80 or better when using only the portion of the forcing that projects onto the first singular vector. Adding the second singular vector adds about 0.07 to the correlation coefficient. Including all the singular vectors would of course bring the total correlation up to 1.0, but none of the singular vectors beyond the second adds more than 0.03 to the correlation (for any of the models.) Table 6 shows the results of the values of the PVI for the SSTA noise case. For all models, 64% (or more) of the variance was induced by projections onto the first singular vector alone, and at least 75% of the variance was induced by the first two singular vectors. In no case did the third, or any subsequent singular vector increase the PVI by more than 4%.

From these two tables, it can be concluded that the perturbations in the shape of the first singular vector cause most of the variation in the Niño-3 index, while the second singular vector is of secondary (but not insignificant) importance. (Recall from TB2000 that these first two singular vectors together represent approximately the real and imaginary phases of the adjoint of the model.) No other individual singular vector seems to be important for explaining the variance produced in the models when driven by temporally and spacially uncorrelated noise.

c. Power spectrum of the pure ENSO mode

Figure 4 showed the power spectra produced by each of the models under stochastic SSTA forcing. The N.97, T.97, and T.80 models showed a distinct pattern with a primary peak near the ENSO period for the model, along with a secondary peak at about 1.5 or 1.3 yr. An examination of a typical Niño-3 index for a pure, neutralized, ENSO mode (see Fig. 1 from TB2000) shows that, even in a pure ENSO mode, more than a single frequency exists.

To see if the secondary peaks are part of the ENSO mode, the spectrum of ENSO mode for each of the models was calculated. In each case, the ENSO mode was initiated at the peak of a warm event and run for 50 yr with no stochastic forcing. The spectra produced (Fig. 10) look remarkably like their respective spectra from the stochastic runs (Fig. 4). Naturally, the power of the pure ENSO mode spectrum is smaller than the forced runs since the ENSO mode decays (quite rapidly in the case of the T.80 and T.60 models). However, the locations of the peaks, and general shape of the curves are the same for the pure modes and the simulations. Perhaps this should not be surprising, since the sto-

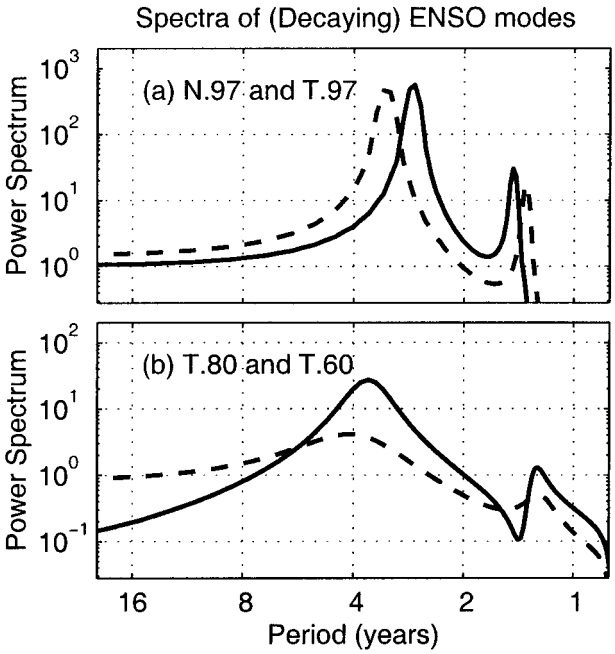

FIG. 10. Spectra of the decaying ENSO modes. Spectra of the Niño-3 index due to a pure ENSO mode (allowed to decay) in each of the models. (a) The N.97 model, dashed line, and the T.97 model, solid line. (b) The T.80 model, solid line, and the T.60 model, dashed line.

chastic simulations seem to consist primarily of the sum of many instances of the ENSO mode, which are stimulated by noise projecting onto the first singular vector, and then decay. For each model, the first singular vector develops quickly (3 months or less) into essentially the pure ENSO mode (Thompson 1998a).

The secondary peaks in the spectra are a result of the annual cycle in the background, and there is a precise mathematical relationship between the frequency of the primary and secondary peaks. Specifically, if p_1 is the period of the primary peak, the period of the secondary peak, p_2, is determined by

$$\frac{1}{p_1} + \frac{1}{p_2} = 1. \tag{4}$$

This relationship, sometimes called unit complementary, has implications for the persistence (spring) barrier that will be discussed in section 5f.

d. Seasonal patterns of variance of the ENSO mode

Figure 5 showed the standard deviation of the Niño-3 index over the 1000-yr simulations on a month by month basis for each model. In TB2000 it was proposed that the tendency of the singular vectors to produce peaks during the winter months would cause the stochastic models to have larger variance during the winter. In section 2 it was indeed shown that the stochastic models tended to peak during the winter—but is the nature of the singular vector growth the reason, or is this a characteristic of the ENSO mode itself? Referring to Fig. 1 of TB2000, notice that like the stochastically perturbed cases, the neutralized ENSO mode also has a tendency to peak in magnitude during winter.

To test this idea, a monthly standard deviation graph was produced for the neutralized ENSO mode of each of the four candidate models, and the results are plotted in Fig. 11. The ENSO modes were ''neutralized'' by increasing the amplitude of the state variables at each time step by enough to compensate for the exponential decay of the mode. The amplitude of the neutralized ENSO modes was set so that the annually averaged variance in the Niño-3 index matches observations. The similarity of the curves in Fig. 11 to those from the stochastic run in Fig. 5 suggest that the nature of both the ENSO mode and the transient growth contribute to the annual cycle of variance. The fundumental reason that both the singular vectors and the ENSO mode tend to peak in the winter months is due to favorable growth conditions from June to November (see Chen et al. 1997 and Thompson 1998a).

e. Which candidate model wins?

The four models derived in TB2000 and driven stochastically in section 2 have been referred to as candidate models—but no judgement has been made about which model most closely matches observations. Eliminating the nearly neutral models, N.97 and T.97, as credible models of nature is fairly easy—they are both too regular. The more damped models, T.80 and T.60, are closer in behavior to the observations. Both the T.80 and T.60 models produce reasonable looking irregularity in the Niño-3 index (Fig. 2). Both models produce spectra that are plausible, except in the neighborhood of a period of 2 yr, where both models are similarly lacking (Fig. 5; but see section 5e). Here T.80 and T.60 have nearly identical seasonal patterns of variance (Fig. 5), and similar autocorrelation statistics (Fig. 6). Altogether, despite having very different damping rates, T.80 and T.60 are nearly equally plausible. However, T.80 does slightly better at reproducing observations in two of the statistics; the power spectrum of T.80 is closer to that of the COADS data (Fig. 4), and the lagged autocorrelation pattern of T.80 is slightly closer to the COADS pattern (Fig. 6). For this reason, the T.80 model has been used as the standard example throughout this paper in cases when a single model is used to demonstrate a point.

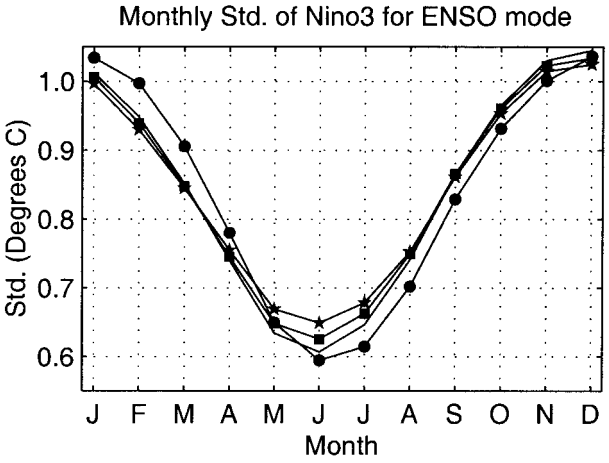

FIG. 11. Seasonal pattern of variance of neutralized ENSO modes. Standard deviation of Niño-3 index due to the pure ENSO mode in each of the models. For each model, the ENSO mode was not allowed to decay, but was instead increased in magnitude at each time step by the appropriate constant factor to keep it neutral. Each ENSO mode was scaled so that its annually averaged variance is the same as the COADS data.

It might seem that T.80 and T.60 have been constructed too similarly for a good study. However, it will be shown in the next section that, despite their apparent similarities, T.60 and T.80 produce very different estimates of the limits of predictability. If the ENSO system is eventually shown to be usefully modeled in this parameter regime (linear and stable), then distinguishing between these two similar models will be important.

4. Limits of predictability

Under the assumption that the above models reflect to some degree the physics of the real system, they will be used to estimate the predictability of the real system.

Most of the studies on ENSO predictability have emphasized the idea that error in the initial conditions is the main source of forecast error (e.g., D. Chen et al. 1995 or Chen et al. 1997). While initial error is important, Fig. 9 suggests that the major player in limiting potential predictability will be the random forcing that occurs between the prediction time and the forecast time (see also Kirtman and Schopf 1998). This difference in emphasis can be explained by the differences in the models used. Much of the previous research on potential predictability has been done with the Zebiak–Cane model, a model in which the system irregularity is attributed to chaos, and hence the concern about the sensitivity to the initial conditions. Kirkman and Schopf, however, use a nonlinear intermediate model that is only slightly unstable and produces a regular periodic, ENSO mode. Their model is made irregular by imposing random external (uncoupled) forcing.

The studies in this section will be concerned with estimating the potential predictability of the Niño-3 index, where the potential predictability is defined as the predictability of the system once the physics has been well characterized, and assuming that observation and data assimilation techniques are sufficiently advanced that initial errors are negligible. This potential predictability will be calculated by using the model to hindcast a time series generated by the model itself. These experiments do assume that the stochastic forcing is completely unpredictable. Since the weather is somewhat predictable for up to two weeks, this assumption is incorrect, but this error is small considering the forecast lengths in question.

a. Annually averaged potential predictability

A predictability experiment is conducted as follows: (i) generate long sample (control) runs using each of the four models with imposed stochastic forcing, (ii) use each model to hindcast it's own control run. The hindcasts are initialized without error, the initial conditions being perfectly known from the control run, and then the model is integrated forward with the external forcing omitted. Using this method, a set of potential predictability limits can be generated: the model physics is perfect, the initial conditions are perfect—forecast errors are caused only by the noise, which is assumed to be unpredictable. In this section the 1000-yr simulations from section 2 were used as the control runs.

Figure 12 shows the correlation coefficient of the Niño-3 index and the rms error for each of the candidate models for prediction periods of up to 36 months. As it might be expected, the predictability is lower for the more damped (and therefore more irregular) models. At 18 months, for instance, the correlation coefficients for N.97 and T.97 are still both greater than 0.9, but T.80's correlation has dropped to about 0.7 and T.60's correlation has dropped to about 0.4. Similarly the (normalized) rms error for the nearly neutral models, N.97 and T.97, is still quite low at 18 months, about 0.35°C. Whereas, the rms errors at 18 months for T.80 and T.60 are 0.7°C and 0.9°C, respectively.

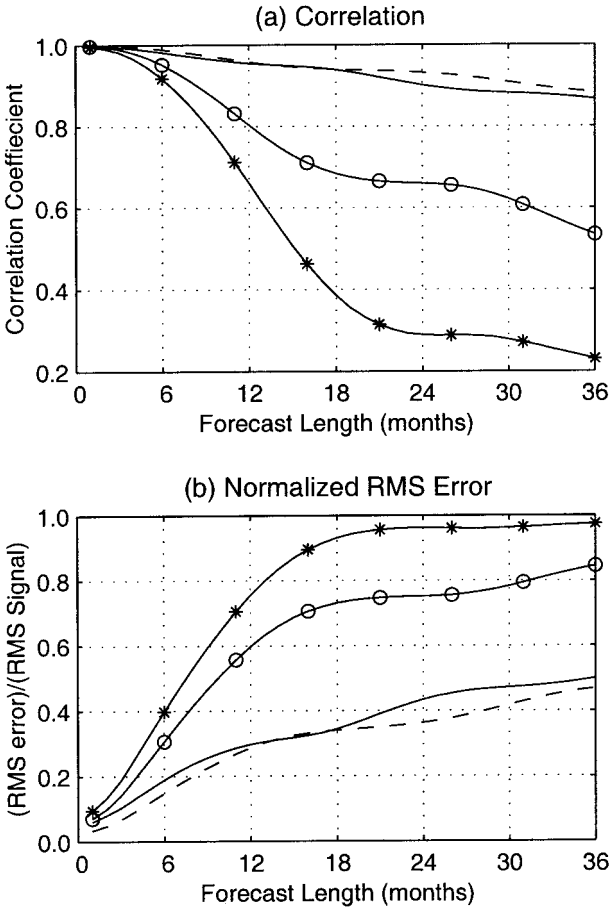

FIG. 12. Averaged potential predictability limit. (a) Shows the correlation of the Niño-3 index obtained from a simulation with the Niño-3 index forecast using the same model with perfect initialization, but without knowledge of future noise forcing. (b) The average normalized rms error for the same forecasts. The key for both (a) and (b) is as follows: the solid line is N.97; the dashed line is T.97; the circles are T.80; the asterisks are T.60.

While it is not surprising that T.80 and T.60 have much lower predictability than N.97 and T.97, it is interesting that there is such a difference in predictability between T.80 and T.60. If one defines the limit of predictability to be the forecast length where the correlation coefficient is less than 0.6, and the rms error greater than 0.8°C, then T.80 has a 30-month predictability limit, while T.60 limit is only 13 months. Yet, the statistics from sections 2 and 3 show that it would be difficult to distinguish these two models from each other using only a short sample of their output. For instance, the two models have very similar envelopes of the Niño-3 index power spectra for 42-yr samples (Fig. 4). Likewise, the annual cycle of variance (Fig. 5), and the autocorrelation patterns (Fig. 6) are quite similar for the two models.

A second set of forecast experiments was run to test

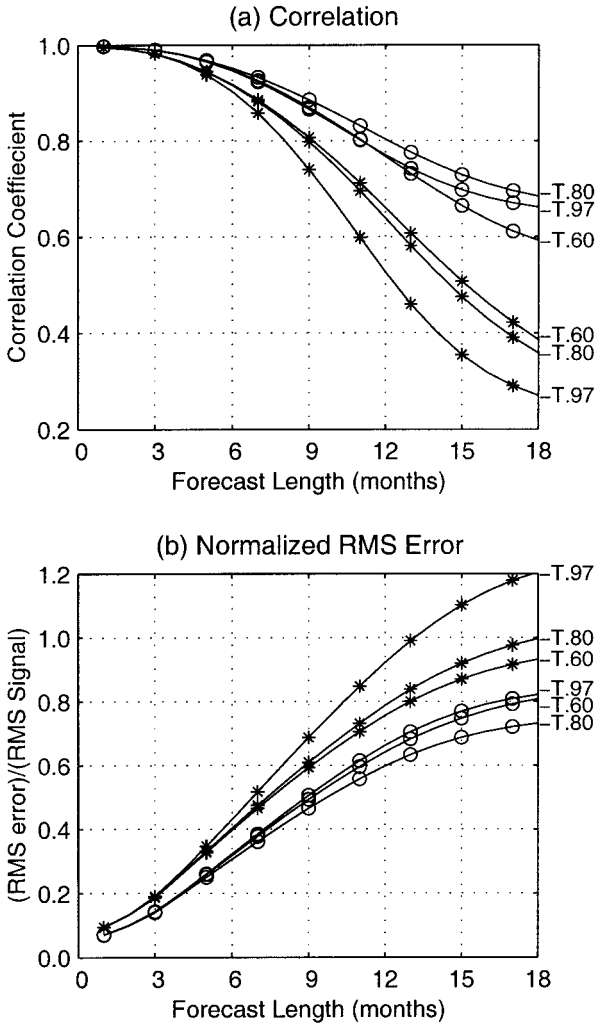

FIG. 13. Imperfect model predictions. These graphs show the results of using one model to forecast the simulated data produced by a different model. The Niño-3 index has been used at the metric to evaluate skill. (a) The correlation for forecasts of the T.80 simulated data (circles) using the T.97, T.80, and T.60 models. Perfect initial conditions were used to start the forecasts, and hence the two sources of error are (i) errors due to the inherently unpredictable future noise and (ii) errors due to differences between the forecast model and the simulation model. The forecasts are repeated using the T.60 model to simulate the data (curves marked with asterisks). (b) Same as (a) except the rms error is measured instead of correlation.

the ability to distinguish between different models. The output of the T.80 and T.60 models were treated as ''observations'' and then the T.97, T.80, and T.60 models were used to hindcast these sets of observations. The question that this experiment addresses is: if one is trying to determine the stability of the system (and ultimately the predictability) by hindcasting observations with a model, then how much better would an accurate model be, compared to a competing inaccurate model? Figure 13 shows the results of these ''imperfect'' model experiments for hindcasts up to 18 months long. Once again, perfect data assimilation was assumed, so the

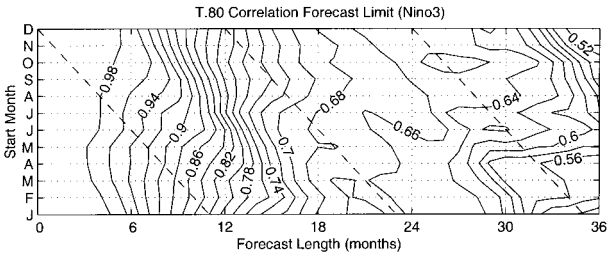

FIG. 14. Seasonal correlation coefficients of T.80 hindcasts. This graph shows the correlation between the T.80 simulation and forecasts of the Niño-3 index in that simulation using the T.80 model, separated by the start month of the forecast. The contour increment is 0.02. The dashed lines indicate where the forecast end time is 1 Jan.

cases of T.80 hindcasting T.80, and T.60 hindcasting T.60 produce the same results as the self-forecasting experiments of Fig. 12.

From Fig. 13, it can be seen that when hindcasting the T.80 data, either the T.60 model or the T.97 model does nearly as well as T.80 itself. At 18 months the correlation coefficient for T.80 self-forecasting is 0.7, while the T.60 has a 0.6 correlation and T.97 has a correlation of 0.66. The rms error of the forecasts at 18 months are also close, ranging from about 0.7°C to 0.8°C. The hindcasting of T.60 data shows that while it might be possible to distinguish the T.97 model from the other models, the T.80 model hindcasts almost as well as T.60 itself. The difference in hindcasting skill at 18 months between T.80 and T.60 being only about 0.03 in the correlation coefficient and 0.07°C in the rms error.

This experiment shows that even though T.80 and T.60 have quite different limits of potential predictability, it will be difficult to distinguish between these models by the differences between the skill of their forecasts, especially given the length of the available data. Therefore, even though a model may do a reasonable job at predicting coarse features of the ENSO cycle (like whether or not next year will be a cold or warm event), it may not produce a correct estimate of the true potential predictability limit.

b. Seasonal predictability

The presence of a strong annual cycle in the singular values (TB2000) suggests that there may be some interesting seasonal structure in the predictability limit in these models. The seasonal cycle of the predictability is studied by examining the rms errors and correlation coefficients-as a function of start month and forecast length in the ''self-forecasting'' experiments. Figure 14 shows the correlation map for the T.80 model, while Fig. 15 shows the rms error map for T.80.

As expected, there is a gradual loss of predictability as the forecast length increases, but Fig. 15 shows there is a larger rate of loss over the (boreal) summer following the first winter after the forecast start time. (The

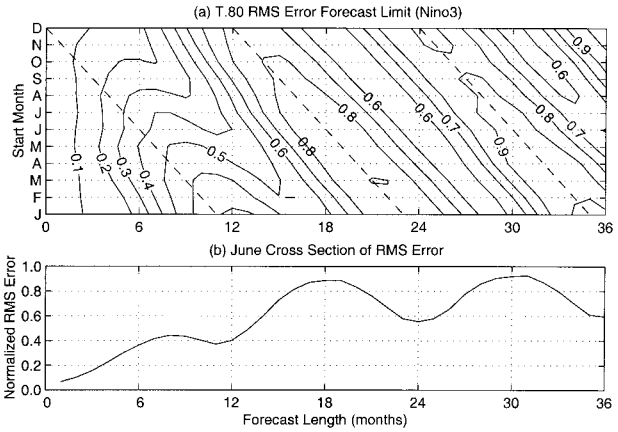

FIG. 15. Seasonal rms errors of T.80 hindcasts. (a) The normalized rms error for forecasts of the Niño-3 index of the T.80 simulation made using the T.80 model, separated by the start month of the forecast. The contour increment is 0.1°C. The dashed lines indicate where the forecast end time is 1 Jan. (b) The Jun cross section of (a).

dotted lines in Figs. 14 and 15 mark the combinations of start month and forecast length that add up to a forecast time of 1 January, therefore this first summer is midway between the first two dashed lines.) This loss in forecast skill is similar to the loss in the autocorrelation occurring during the summer months (Fig. 6). The other models show a similar predictability loss during the summer, though it is more pronounced in N.97 and T.97 and less pronounced in T.60 (not shown).

This pattern can be attributed more to the nature of the ENSO cycle than to the nonuniformity of the singular value maps. Since the ENSO mode tends to peak in winter, to get a good *correlation* in the winter it is important to get the sign of the prediction right—if the amplitude is close, then the correlation will be high. However, in this model, the ENSO mode is generally in transition between warm and cold events during the late spring/early summer. At this time the amplitude will be close to zero, and the slope of the Niño-3 index will be at its greatest. A minor misprediction of the timing of the transition will lead to a large-amplitude error or even a misprediction of the sign.

The rms error map, Fig. 15, also shows a strong seasonal structure. For the longer forecast times (by the second winter), a yearly cycle is discernible: the predictability is better for forecasts ending at the beginning of summer and worsens for forecasts of wintertime anomalies. This structure in the rms map can largely be accounted for by the annual cycle of variance (Fig. 5). For forecast times past the second winter, the model is doing little better than making random guesses: the seasonal cycle in the rms error is just a reflection of the fact that both the forecast model and the data have lower variance in the summer. The effect is subtler for shorter forecast times, since the slope of the overall increase in rms error is large, but the effect can still be seen in the T.80 rms error map.

5. Discussion

a. The irregularity of ENSO

Numerous mechanisms have been proposed for the irregularity of ENSO. One hypothesis is that the irregularity of ENSO is due to intrinsic nonlinearity in the coupled atmosphere–ocean system (including ENSO), which operates even in the absence of any annual cycle, or in the interaction between ENSO and other modes of variability. Other investigators have explored the interactions between ENSO and the seasonal cycle (e.g., Chang et al. 1994; Jin et al. 1996) as the root cause of the irregularity of ENSO. Unfortunately, the behavior of the models in these theories does not match well with the observations (see Neelin et al. 1998 for an overview).

Many investigators have put forth coupled models in which (i) the coupling strength is sufficient to create an ENSO mode—the leading mode of the coupled atmosphere–ocean system—which is linearly unstable, and (ii) nonlinearity acts only to limit the amplitude of the oscillations and does not create irregularity (e.g., Shopf and Suarez 1988; Battisti and Hirst 1989; Eckart and Latif 1997; Chang et al. 1996; Blanke et al. 1997; Flügel and Chang 1998; Kirtman and Schopf 1998). In each of these studies, the irregularity of ENSO is attributed to stochastic forcing that is envisioned to be due to variability in the atmosphere (e.g., weather), which is unrelated to the changes in the SST.

Recently, several investigators have discussed the possibility that ENSO may be described as a coupled dynamical system and that both the irregularity *and* the occurrence of ENSO are due to stochastic forcing of the coupled system (e.g., Penland and Sardeshmuhk 1995). In this view of the system, the dynamics are linear but the coupled system is globally stable to perturbations and ENSOs come about because of noise forcing on the system. Blanke et al. (1997) and Chang et al. (1996) stabilized hybrid coupled atmosphere–ocean models[2] and forced them with a stochastic temporal representation of the residual patterns of wind stress (i.e., the observed wind stress patterns not related linearly to the observed SST anomalies) and concluded that a stochastic linear hypothesis for ENSO was possible

[2] A coupled atmosphere–ocean model that uses a dynamical ocean model (either a GCM or a reduced gravity representation of the ocean dynamics) coupled to an empirical atmosphere model is called a ''hybrid coupled model.'' The empirical atmosphere model is a model of the equilibrium state of the atmosphere to the observed SST distribution. It is usually built by taking linear regressions between the time series of the observed monthly averaged patterns of SST and the time series of the leading patterns of wind stress and heat flux anomalies. See Barnett et al. (1993) for an example.

(though Blanke et al. felt it was a weaker hypothesis than the unstable linear hypothesis). Jin et al. (1996) argued that the stable linear hypothesis for ENSO was less likely that the linear unstable hypothesis because of an absence of a quasi-biennial peak in their simulation (but see the end of section 5f). Penland et al. (2000) build a linear inverse model of the historical SST data in the Indo-Pacific region, and compare the statistics of that model to those generated from a hybrid model of the coupled atmosphere–ocean system in the tropical Pacific; experiments with the later model are carried out in various parameter regimes including: very stable quasi-linear, stable quasi-linear, and unstable nonlinear. They conclude that ENSO is most likely to reside in a stable dynamical regime.

The results presented herein support the hypothesis that ENSO is due to stable linear coupled dynamics. Specifically, this paper demonstrates that in this hypothesis for ENSO the most slowly decaying (Floquet) mode of the coupled system is the ENSO mode, realized by the same physics as the ENSO mode in the linearly unstable models: the so-called linear delayed oscillator physics, as describe in Battisti (1988) and Battisti and Hirst (1989). Furthermore this study shows that the tendency for ENSOs to peak at the end of the calendar year is explainable from the seasonality in the dynamics of the system (i.e., the strong annual cycle of the climatological mean state) and does not require seasonality in the stochastic forcing (cf. Penland and Sardeshmukh 1995) or, for that matter, any special structure in the stochastic forcing (e.g., the intraseasonal, or Madden–Julian, oscillation) to produce realistic levels of ENSO variability.

b. Stability, singular values, predictability, and forcing amplitude

It seems intuitive that the amplitude of the stochastic forcing on a model would be the primary determinant of the model's predictability. However, for these models, this is not the case. For instance, N.97 has nearly twice the stochastic forcing of T.97, but the two models have nearly identical predictability characteristics (see Fig. 12). The reason is that N.97 has much smaller singular values than T.97 (see Table 1 and TB2000). Most variability in these models is produced by the noise projecting onto the first singular vector that then grows by the magnitude of its singular value (in the L2 norm; Thompson 1998a). The amplitude of the stochastic forcing required to sustain a given variability is also strongly affected by the model's asymptotic stability. For instance, T.97 and T.80 have nearly the same sensitivity to stochastic forcing (since their singular values are similar) but T.97 requires less than half the forcing of T.80 to sustain the same variability. Therefore, the amplitude of variability produced by each model is determined by the combination of its singular values, its stability, and the amplitude of the imposed stochastic forcing.

Each model's predictability is primarily determined not by the stochastic forcing or singular values, but by its stability. Since the system variability is fixed, one might also say that the combination of forcing amplitude and singular values determines predictability. But suppose the stochastic forcing were allowed to increase by 20%—would not the predictability degrade? No—in a linear system, the predictability remains unchanged. The overall system variability increases by 20%, but correlation prediction skill and (normalized) rms error of prediction would remain the same. This is not true, in general, for a nonlinear system. In particular, in a system at or near saturation, increasing the forcing decreases the predictability while only slightly increasing the variability.

c. Why ENSO tends to peak in boreal winter

There is a remarkable tendency for the extrema of ENSO events to peak around the end of the calendar year—so much so that Rasmusson and Carpenter (1982) discussed a canonical ENSO that was an average of six warm ENSO events, composited about the annual cycle. Wallace et al. (1998) show that this tendency is robust throughout most of the observation record (1854–1995). Numerous studies have discussed potential mechanisms by which this phase locking[3] may come about. For example, Clarke and van Gorder (1999) postulate a nonlinear interaction between ENSO and an (undefined) biennial signal is the root cause of the phase locking. Alternatively, Jin et al. (1996) find that if the system is highly unstable to small perturbations, nonlinear interaction between the ENSO mode and the annual cycle can cause the phase locking of ENSO, albeit with highly unrealistic overall temporal characteristics (cf. their Figs. 15, 8c, and 8d).

Penland and Sardeshmukh (1995) suggest ENSO is determined by linear dynamics that are independent of the seasonal cycle, and the phase locking of ENSO is due to seasonality in the stochastic noise forcing of the coupled system. Upon further analysis of the observations, however, Johnson et al. (2000) have shown that there is significant seasonality in the coupled dynamical operator, though they did not attempt to define what was more important for the ENSO phase locking, seasonality in dynamics or in the stochastic forcing of the system.

The results of this study indicate that the large seasonality of ENSO can be generated by the annual cycle in the coupled dynamics, even without a seasonal cycle in the noise that is used to force the system. Specifically, the annual cycle in the climatological averaged fields gives rise to seasonality in the coupling strength; hence, the leading mode of the system (the ENSO mode) has

[3] In this paper, the tendency of ENSO events to peak at the end of the calender year will be referred to as phase locking (i.e., the ENSO cycle is phase locked to the annual cycle).

a tendency to peak at the end of the calendar year (see Fig. 5).

To be sure, these model results are deficient in that the minimum in the annual cycle of ENSO-related variance occurs about three months later than in the observations (i.e., in June rather than March), and the decline in variance from January to March in the model is not as precipitous as in the observations. These problem are probably due to one or more of four things: (i) errors in the prescription of the climatological annual cycle of currents and winds; (ii) too crude treatment of the surface heat flux anomalies associated with anomalies in SST; (iii) nonlinear processes; and (iv) the approximation of the ocean as a 1.5-layer system. Experience with the model shows that it would have been relatively easy to ''tweak'' the model's mean fields (within observational uncertainty) and remedy these model deficiencies, but this kind of manipulation is arbitrary and a nonunique way to ''fix'' these discrepancies. In any case, these model deficiencies do not affect the conclusion that it is likely that seasonality in the linear dynamics plays a large part in phase locking ENSO to the annual cycle.

d. The ''decadal'' variability of ENSO

Zhang et al. (1997) showed that there is pronounced variability in the pan-Pacific atmosphere and ocean that is very similar in structure to the interannual ENSO phenomenon but the time series of this ENSO-like pattern of climate anomalies features variability that is on timescales of many years to decades, albeit with occasional rapid changes (including notable ones in 1942–43 and 1976–77). From Figs. 4c and 4d, it is clear that the linear stable stochastically forced coupled atmosphere–ocean system supports variability of ENSO that is statistically indistinguishable to that observed on all timescales longer than two years—including on the decadal timescale. Hence, our results are consistent with the conclusions reach by Zhang et al. that the low-frequency ENSO-like variability can be thought of as being essentially the residual that comes from averaging the variability over time periods that are longer than one oscillation of the (decaying) ENSO mode. The subtle differences in the structure of the SST patterns associated with the interannual ENSO mode and the low-frequency ENSO-like variability can be attributed to (i) the frequency dependence of the critical latitude for zonal propagation of oceanic Rossby waves off an eastern boundary (e.g., Gill 1982) and (ii) the amplification of the SST anomalies in midlatitudes at the lower frequencies associated with the teleconnected atmospheric forcing (via the atmospheric bridge; Lau and Nath 1996). See Zhang et al. (1997) for a more complete discussion.

Several additional mechanisms have been hypothesized to explain the decadal-scale ENSO-like variability. One such hypothesis suggests that decadal ENSO-like variability is generated by an atmospheric forcing present during an extended ENSO event that creates thermal (Gu and Philander 1997) or circulation (McCreary 1983) anomalies in the subtropical eastern Pacific Ocean. Such anomalies are subducted and ''teleconnected'' by the ocean circulation to the equatorial western Pacific, where they enter the tropical waveguide, terminate the ENSO event, and flip the system into an extended ENSO event of the opposite sign. The decadal timescale follows from the long transit time for the oceanic teleconnection. Observations suggest there are several difficulties with this hypothesis (see Schneider et al. 1999), but the most notable is the lack of any bimodal structure in any indexes of ENSO. Furthermore, Penland and Sardeshmukh (1995) performed a careful analysis of the observed Niño-3 index that supports the hypothesis that much of the relevant dynamics are dominated by Gaussian dynamics, except during the peak of ENSO warm events (see also Burgers and Stephenson 1999, and section 5e).

As might be expected due to the strong annual cycle in the variance of ENSO, there is a strong annual cycle in lagged autocorrelation (persistence) in various indices of ENSO—the so-called spring barrier (see Fig. 6). Flügel and Chang (1999) use approximately 20-yr windows for calculating the annual cycle of the autolag of SST. They find that the spring barrier is a robust feature throughout the period 1900–76. During the period 1977–92, however, there was a much weaker annual dependence in the lagged autocorrelation. Several studies have hypothesized that this change in the spring barrier is due to slow changes in the basic state of the tropical Pacific (e.g., Kirtman and Schopf 1998), which then affects the growth and period of the ENSO mode as well as its predictability. The model used in this study shows similar behavior: the spring barrier disappearing for decades at a time (see Fig. 7). However, in this model there is no change in the basic state, and this decadal variability in the spring barrier is seen to be a statistical artifact of a short sampling interval that does not reach stationarity in the statistics.

e. The role of nonlinearity

Burgers and Stephenson (1999; hereafter BS99) have analyzed the probability distribution function of various indices of ENSO to determine the extent to which nonlinearity is important. They conclude that several common indexes of ENSO are distinguishable from a Gaussian distribution; these include Niño-3.4, Niño-4, and (Fraedrich 1988; Stephenson 1997) the Southern Oscillation Index (SOI). In the eastern Pacific, however, BS99 find the SST changes associated with ENSO do indicate a local nonlinearity, as suggested by a skewness of 0.86 in the Niño-3 index.

The root model for the linear coupled models analyzed in the present paper is Battisti's (1998) version of the Zebiak and Cane (1987) model; the differences be-

tween the root model and the four models in the present paper are (i) the root model is nonlinear and is in a linearly unstable regime, and (ii) key parameter values have been modified to build the four linearly stable models: T.97, N.97, T.80, and T.60 (see section 1 and Table 2).

Two additional experiments were performed using Battisti's (nonlinear) model with the T.80 parameter set. First, the model is integrated without external noise forcing; as expected, the model does not sustain an internally generated variability. Next, the same nonlinear T.80 model is integrated using the same stochastic forcing that was applied to the (linear) T.80 model. The question being addressed is whether the nonlinear extension of the linear model with a realistic set of parameters (e.g., the T.80 parameter set) is consistent with the analysis of the observations reported in BS99.

The nonlinear model with the T.80 set of parameters, when stochastically forced, reproduces all of the basic features from the linear models: ENSO is the dominant mode of variability (with realistic amplitude); ENSO events tend to peak at the end of the calendar year and evolve through the same physics (the so-called delayed oscillator physics) as in all the linearized models and in the unstable nonlinear model (Battisti 1988). Clearly, the essential characteristics of ENSO appear to be governed by linear processes.

Though nonlinearity plays a secondary role in the nonlinear T.80 model, it is important in the cold tongue region of the eastern Pacific (consistent with observations; BS99) where it serves to modify the amplitude of the extreme warm and cold phases of ENSO (via horizontal advection and upwelling; see Battisti 1988). From a nonlinear T.80 model run of 440 yr, the skewness in Niño-3 is calculated to be 0.31, and the reduced kurtosis is -0.38. Hence, warm extremes are more likely to occur than cold extremes, and the distribution is somewhat flatter than Gaussian. Using BS99's criteria for estimating the 95% confidence level, the simulated Niño-3 index is indistinguishable from that estimated from COADS (the observed Niño-3 features a skewness of 0.57 ± 0.5 and a reduced kurtosis of 0.09 ± 0.7).

f. The cause of the spring barrier

The hypotheses for the spring barrier in the lagged autocorrelation that is evident in many indexes of ENSO (e.g., Niño-3, SOI) fall into two generic categories: (i) ENSO exists in the presence of some other mode of climate variability that has a biennial timescale (e.g., Clark and van Gorder 1999; Meehl 1997); (ii) ENSO is intrinsically stable and there exists important seasonality in either the uncoupled forcing (e.g., Penland and Sardeshmukh 1995) or the ENSO dynamics (e.g., this study; Johnson et al. 2000), or both, that is responsible for the spring barrier. Next these hypotheses are examined in light of the results from the T.80 model, along with the original nonlinear model updated to use T.80 parameter set. Figure 16 shows the Niño-3 lagged autocorrelation from (a) observations, (b) the linear T.80 model, (c) the nonlinear T.80 model under small amplitude noise, and (d) the nonlinear T.80 model under full noise forcing. In all cases the forcing is applied to the SST and it is white in space and time; ''full noise'' means the noise is the same as is applied to the linear T.80 model, while ''small amplitude noise'' is reduced to 10% of the full noise case.

Figure 16 suggests that the basic mechanism behind the observed spring barrier is the linear physics of the ENSO mode because of the annually varying basic state. An annual cycle in the noise forcing is not required for the presence of the spring barrier, consistent with the analysis of the observations by Johnson et al. (2000; see also Torrence and Webster 1998). The same analysis of the nonlinear T.80 model under small and full noise forcing shows that, when the forcing is large enough to generate realistic amplitude variance in Niño-3, the spring barrier becomes sharper (cf. in Figs 16b,c, and d) and is somewhat more consistent with observations: compared to the linear model, in the nonlinear model the barrier shifts to slightly earlier in the year and the negative correlations at long lag are small.

It is interesting to note that the mathematical characteristics of a system that displays a barrier in lagged autocorrelation has been explored in recent studies. Weiss and Weiss (1999) found that a time series having either enhanced biennial power (see below) or spectral peaks at frequencies that are unit-complementary will have an annual cycle barrier in lagged autocorrelation. As noted in section 3c, the models in this study display pairs of spectral peaks that are unit-complementary. The difference in the ENSO mode between the study of Thompson (1998a), which uses a constant mean state, and this study, which uses a cyclic mean state, suggest that the unit-complement is a result of the linear ENSO physics evolving on the annually varying mean state.

The effects of nonlinearity on the spectrum of the ENSO mode were examined using Niño-3 as a proxy index of ENSO. Figure 17 shows that, compared to the linear model, nonlinearity enhances the variability at timescales longer than $\sim$8 yr and in the biennial band.[4] Hence, the spectrum is somewhat flattened compared to the linear case.

A major deficiency in the linear model was a statistically significant underestimate of the power in the biennial band (see Fig. 4). Though the essential physics of the model ENSO is linear (even in the unstable parameter regime; see Battisti and Hirst 1989), when the

[4] Because we have 500 yr of model data in the nonlinear runs [or 1000 yr in the linear runs], the differences in the model spectrum in these frequency bands are statistically significant. However, for long timescales [8 yr or more], the observed spectrum of the Niño-3 index is indistinguishable from that obtained from both the linear or nonlinear model.

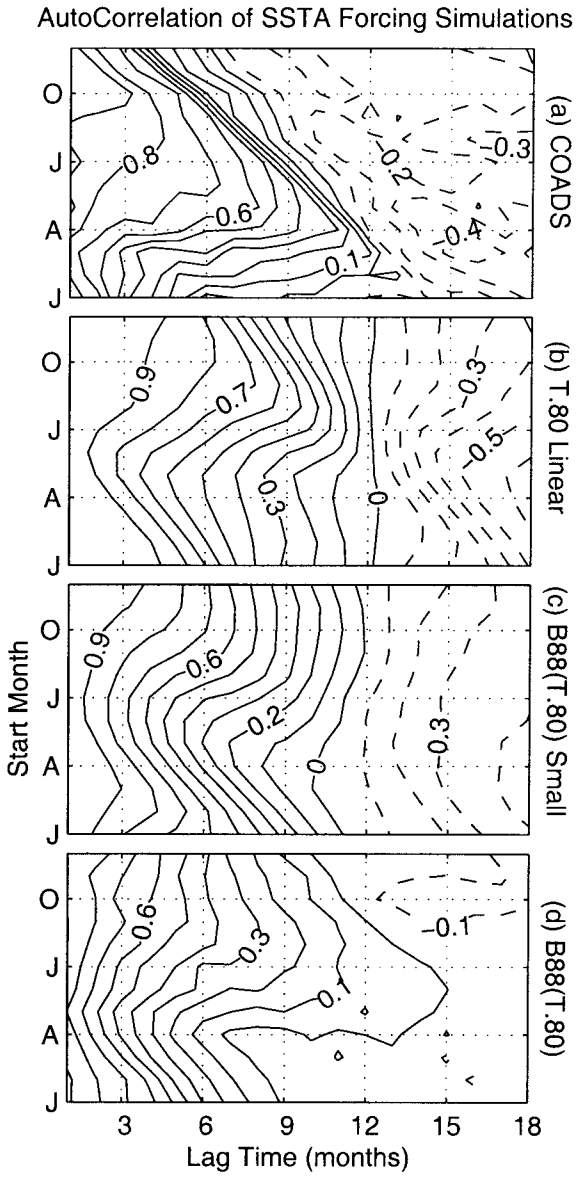

FIG. 16. Autolag correlation of Niño-3 from observations, and from the linear and nonlinear simulations using the T.80 parameter set. Autolag correlation starting at each month of the year out to lag times of 18 months. (a) COADS, while (b) reproduces Fig. 6d for the linear T.80 model. (c)–(d) The nonlinear version of the coupled model (the B88 model) with the T.80 parameter set. All models undergo stochastic forcing that is uniformly distributed in space and time (white). The amplitude of the forcing applied to the linear T.80 (b) and the ''full amplitude'' run of the nonlinear T.80 model (d) is identical. (c) The results from the nonlinear T.80 model when the forcing has been reduced to have 10% amplitude (1% power) compared to that used in full amplitude forcing. The variance of Niño-3 in the linear, ''small amplitude'' nonlinear and full amplitude nonlinear models is 0.72, 0.01, and 0.91 K^2, respectively. Contour interval is 0.1 for (a)–(d).

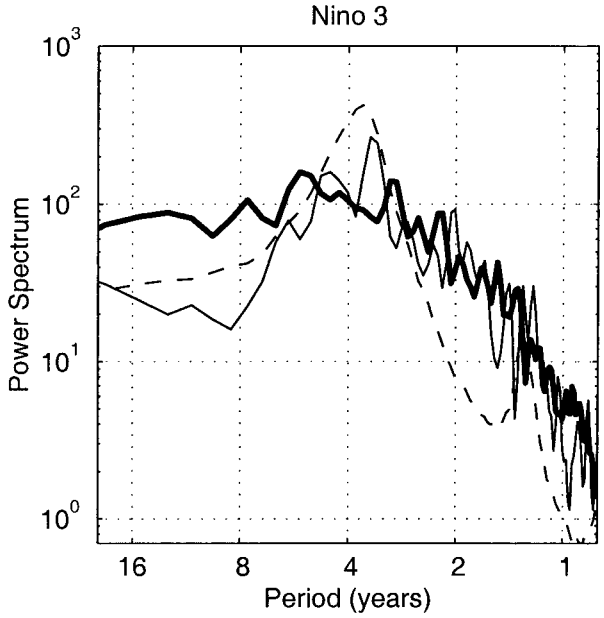

FIG. 17. Power spectra of Niño-3 from COADS and the linear and nonlinear coupled models with the T.80 (more realistic) parameter set. The thick solid line (dashed line) is for the nonlinear (linear) model under the same amplitude stochastic forcing. The thin dashed line is observations (COADS). The error in the observed spectrum can be estimated from the dashed lines in Fig. 4.

nonlinear model is forced by sufficient noise to exhibit realistic amplitude variability, the nonlinearity becomes important at the extrema of ENSO (e.g., Battisti and Hirst 1989), and results in an enhancement of the power in the biennial band (compared to the linear model), which is now consistent with that observed.

As biennial power has also been shown to be a characteristic of a system that supports an annual barrier in lagged autocorrelation (Weiss and Weiss 1999; Clarke and van Gorder 1999), it is not surprising that the nonlinear model has a somewhat sharper spring barrier than that of the linear model (cf. Fig. 16d with either 16b or 16c). However, it is emphasized that in the present study the biennial power is inherently due to nonlinearity that acts to enhance the tendency for ENSO to be coordinated with the annual cycle (so warm events are confined to lasting about 1 yr, and are usually followed by cold events for the following year); there may be other sources of biennial variability in the tropical Pacific that are in addition to, and separate from, that which is intrinsic to ENSO (e.g., as postulated by Meehl 1997; or Clarke et al. 1998).

6. Conclusions

In Part 1 of this study (Thompson and Battisti 2000) Floquet analysis was used to examine the leading mode in the linearized version of a variant of the Zebiak and Cane (1987) coupled atmosphere–ocean model. This leading mode is the model's version of ENSO, and is

characterized by the so-called delayed oscillator physics as described in Battisti (1988) or Battisti and Hirst (1989). In the model, the structure and evolution of key variables (e.g., SST, thermocline, and zonal wind stress) are broadly consistent with those observed; the frequency of the ENSO mode is commensurate with the weak spectral peak that is ubiquitous in tropical Pacific climate indexes. It was also demonstrated that, because of the annual cycle in the mean fields (and hence in the coupling strength), perturbations imposed on the system achieved greatest amplification if they were applied in boreal spring and grew through the following fall and winter. For the standard values of parameters, the ENSO mode is unstable. However, when three important parameters were modified to have more realistic values,[5] the leading Floquet mode (the ENSO mode) had the same structure and physics, but the mode was now rendered linearly stable with a decay rate of roughly 0.75 per year.

In this paper, Part II, the results of Part I have been extended to explore the possibility that the coupled atmosphere–ocean system in the tropical Pacific is linearly stable. In this view, ENSO comes about through stochastic forcing of the coupled atmosphere–ocean system, where the stochastic forcing is envisioned as primarily due to uncoupled atmospheric variability. The same four linearly stable dynamical models developed in Part I were employed—each with different but realistic sets of values for key parameters.

The results of this study suggest that the linear, stable dynamical model of ENSO is indeed a plausible null hypothesis for the observed ENSO. It is shown that this model can produce ENSO events with realistic structure and amplitude. Also consistent with observations is the temporal spectrum of ENSO, featuring a broad spectral peak around 3.5–6 yr (associated with the ENSO mode, i.e., the leading Floquet mode) superimposed on an otherwise red spectrum. Using forcing that is white in space and time, the model exhibits strong seasonality in the occurrence of ENSO and in the lagged autocorrelation of SST (the so-called spring barrier) in the center of action of ENSO. For example, warm and cold ENSO events are shown to peak at the end of the calendar year (as observed) because of the annual cycle in the mean fields.

All four of the candidate models can support the observed level of variance in the coupled system (the ENSO mode) with realistic levels of stochastic forcing. For example, when the stochastic forcing is chosen to be white in space and time, realistic amplitude ENSOs are achieved with SST and thermocline perturbations of the order of 0.25°C and 2 m, respectively, even for a choice of parameter values that damp the system to a highly linearly stable regime. Experiments were run using a variety of prescriptions in the stochastic forcing, including forcing SST only and forcing thermocline only. The structure and temporal properties of the simulated ENSO in the stochastically forced linear dynamical system (including the phase-locking to the annual cycle) are insensitive to the details of the prescribed stochastic forcing. In particular, the results suggest that the phase-locking of ENSO to the seasonal cycle and the spring persistence barrier of ENSO are properties that are intrinsic to the linear physics of ENSO operating under annual variations in the climatological basic state of the ocean and atmosphere [contrasting hypotheses are found in, e.g., Penland and Sardeshmukh (1995) and Clarke and van Gorder (1999)].

An examination was made of the potential predictability of ENSO in the linearly stable coupled system, where potential predictability is defined as the limits of predictive skill of the model (if the initial conditions are known perfectly). Increasing the stability of the ENSO mode yields a system that is governed less by deterministic dynamics than it is by the stochastic forcing of the coupled system. Hence, the potential predictability of ENSO in the linearly stable model is much more modest than in the unstable coupled system. The predictability of ENSO is limited to one year, or less, in a variant of the Zebiak and Cane (1987) coupled model with updated parameters, which is linearly stable to perturbations. A brief examination of the seasonal dependence of forecast skill is presented.

Numerous investigators have reported on the observed variability in the Pacific that has a spatial structure resembling that associated with the interannual ENSO mode, but with characteristic timescales that are longer than interannual. Several studies have hypothesized that this decadal variability may be announcing a new ''mode'' of the coupled system, or an exotic (nonlinear) oceanic teleconnection between the tropical Pacific and the subtropics or midlatitudes (e.g., Gu and Philander 1997). In support of the analysis of the observations and of the accompanying discussion presented in Zhang et al. (1997), this study puts forward evidence for the null hypothesis—that the decadal ENSO-like variability is essentially due to the (uncoupled) stochastic forcing upon the coupled atmosphere–ocean system, confined to the tropical Pacific. This forcing causes a broadening of the spectrum associated with the leading stable (ENSO) mode of the coupled system (see Figs. 4 and 17), including an accumulation of energy at lower frequencies. In this scenario, the subtle differences between the spatial patterns of the variability of SST on the interannual versus decadal timescale are hypothesized to be due to the the frequency dependence of the latitude at which Rossby waves emanate from the

[5] In Part I, three critical parameter values were modified to control for the growth rate and period of the ENSO mode: the coupling strength, the efficiency of the western boundary reflection of incoming Rossby signals, and the mechanical damping time of the ocean. Observational, theoretical, and modeling studies have shown that these parameters should be reduced in amplitude from their values in the original coupled model. The four candidate models were constructed using physically plausible values for these parameters.

western coast of the Americas, and to the amplification of midlatitude SST anomalies (relative to those in the Tropics) that are forced by atmospheric teleconnections from the Tropics (see Zhang et al. 1997 for further discussion).

Though model results and observations indicate the essential physics of ENSO is linear, retaining nonlinear terms in the coupled model with the more realistic parameter set resulted in modest quantitative changes in ENSO. In particular, nonlinearity increases the tendency for warm events to be followed the next year by cold events. Thus, compared to the linear model, nonlinearity acts to enhance power in the biennial band, sharpen the persistence barrier of Niño-3, and shifts the barrier earlier by a few months, to occur in late boreal spring/early summer. However, neither the linear nor the nonlinear model features a spring barrier as intense as is observed.

Finally, the reader is cautioned that these results are obtained with an intermediate coupled atmosphere–ocean model. The design of the model does not admit various physical processes that have also been hypothesized to be important at longer timescales (e.g., basinwide thermohaline circulation and Indonesian throughflow). This research shows that realistic levels of decadal variability can be generated simply by very modest levels of stochastic (uncoupled) forcing of the coupled system in tropical Pacific. Hence, the challenge will be to extract the decadal timescale variability in the system that is due to the more exotic physics from the (large) ubiquitous decadal variability that almost certainly results from uncoupled stochastic forcing of the coupled tropical Pacific system.

Acknowledgments. The authors thank the following people for numerous stimulating discussions during the course of this work: Ping Chang, Ben Kirtman, Ed Sarachik, and Paul Schopf. This work has been supported by a Grant from the NOAA Office of Global Programs to the Hayes Center at the University of Washington.

REFERENCES

Balmaseda, M. A., M. K. Davey, and D. L. T. Anderson, 1995: Decadal and seasonal dependence of ENSO prediction skill. *J. Climate,* **8,** 2705–2715.

Barnett, T. P., M. Latif, N. Graham, M. Flugel, S. Pazan, and W. White, 1993: ENSO and ENSO-related predictability. Part I: Prediction of equatorial Pacific sea surface temperature with a hybrid coupled ocean–atmosphere model. *J. Climate,* **6,** 1545–1566.

Battisti, D. S., 1988: The dynamics and thermodynamics of a warming event in a coupled tropical atmosphere–ocean model. *J. Atmos. Sci.,* **45,** 2889–2919.

——, and A. C. Hirst, 1989: Interannual variability in the tropical atmosphere–ocean system: Influence of the basic state, ocean geometry and nonlinearity. *J. Atmos. Sci.,* **46,** 1687–1712.

Blanke, B., J. D. Neelin, and D. Gutzler, 1997: Estimating the effect of stochastic windstress forcing on ENSO irregularity. *J. Climate,* **10,** 1473–1486.

Burgers, G., and D. B. Stephenson, 1999: The ''normality'' of El Niño. *Geophys. Res. Lett.,* **26,** 1027–1030.

Chang, P., B. Wang, T. Li, and L. Ji, 1994: Interactions between the seasonal cycle and the southern oscillation—Frequency entrainment and chaos in a coupled ocean–atmosphere model. *Geophys. Res. Lett.,* **21,** 2817–2820.

——, L. Ji, H. Li, and M. Flugel, 1996: Chaotic dynamics versus stochastic processes in El Niño-Southern Oscillation in coupled ocean–atmosphere models. *Physica D,* **9,** 301–320.

Chen, D., S. E. Zebiak, A. J. Busalacchi, and M. A. Cane, 1995: An improved procedure for El Niño forecasting: Implications for predictability. *Science,* **269,** 1699–1702.

Chen, Y.-Q., D. S. Battisti, and E. Sarachik, 1995: A new model for the study of the tropical oceanic aspect of ENSO. *J. Phys. Oceanogr.,* **25,** 2065–2089.

——, ——, T. N. Palmer, J. Barsugli, and E. S. Sarachik, 1997: A study of the predictability of tropical Pacific SST in a coupled atmosphere–ocean model using singular vector analysis: The role of the annual cycle and the ENSO cycle. *Mon. Wea. Rev.,* **125,** 831–845.

Clarke, A. J., and S. van Gorder, 1999: The connection between the boreal spring southern oscillation persistence barrier and biennial variability. *J. Climate,* **12,** 610–620.

——, X. Liu, and S. van Gorder, 1998: Dynamics of the biennial oscillation in the equatorial Indian and far western Pacific Oceans. *J. Climate,* **11,** 987–1001.

Eckert, C., and M. Latif, 1997: Predictabilty of a stochastically forced hybrid coupled model of El Niño. *J. Climate,* **10,** 1488–1504.

Flügel, M., and P. Chang, 1998: Does the predictability of ENSO depend on the seasonal cycle? *J. Atmos. Sci.,* **55,** 3230–3243.

——, and ——, 1999: Stochastically induced climate shift of El Niño–Southern Oscillation. *Geophys. Res. Lett.,* **26,** 2473–2476.

Fraedrich, K., 1988: El Niño/Southern Oscillation predictability. *Mon. Wea. Rev.,* **116,** 1001–1012.

Gill, A. E., 1982: *Atmosphere–Ocean Dynamics.* Academic Press, 662 pp.

Gu, D., and S. G. H. Philander, 1997: Interdecadal climate fluctuations that depend on exchanges between the tropics and extratropics. *Science,* **265,** 805–807.

Jin, F.-F., J. D. Neelin, and M. Ghil, 1996: El Niño/Southern Oscillation and the annual cycle: Subharmonic frequency locking and aperiodicity. *Physica D,* **9,** 442–465.

Johnson, S. D., D. S. Battisti, and E. S. Sarachik, 2000: Seasonality in an emperically derived Markov model of tropical Pacific sea surface temperature anomalies. *J. Climate,* **13,** 3327–3335.

Kirtman, B., and P. Schopf, 1998: Decadal variability in ENSO predictability and prediction. *J. Climate,* **11,** 2804–2822.

Kleeman, R., 1993: On the dependence of hindcast skill on ocean thermodynamics is a coupled ocean–atmosphere model. *J. Climate,* **6,** 2012–2033.

Lau, G., and M. J. Nath, 1996: The role of the atmospheric bridge in linking tropical Pacific ENSO events to extratropical SST anomalies. *J. Climate,* **9,** 2036–2057.

Madden, R. A., and P. R. Julian, 1972: Description of global-scale circulation cells in the tropics with a 40–50 day period. *J. Atmos. Sci.,* **29,** 1109–1123.

McCreary, J. P., 1983: A model of tropical ocean–atmosphere interaction. *Mon. Wea. Rev.,* **111,** 370–387.

Meehl, G. A., 1997: The south Asian monsoon and the tropospheric biennial oscillation. *J. Climate,* **10,** 1921–1943.

Moore, A. M., and R. Kleeman, 1999: Stochastic forcing of ENSO by the intraseasonal oscillation. *J. Climate,* **12,** 1199–1220.

Neelin, J. D., D. S. Battisti, A. C. Hirst, F. F. Jin, Y. Wakata, T. Yamagata, and S. Zebiak, 1998: ENSO Theory. *J. Geophys. Res.,* **103,** 14 261–14 290.

Penland, C., and P. D. Sardeshmukh, 1995: The optimal growth of tropical sea surface temperature anomalies. *J. Climate,* **8,** 1999–2024.

——, M. Flügel, and P. Chang, 2000: Identification of dynamical

regimes in an intermediate coupled ocean–atmosphere model. *J. Climate,* **13,** 2105–2115.

Schneider, N., S. Venzke, A. J. Miller, D. W. Pierce, T. P. Barnett, C. Deser, and M. Latif, 1999: Pacific thermocline bridge revisited. *Geophys. Res. Lett.*, **26,** 1329–1332.

Schopf, P. S., and M. J. Suarez, 1988: Vacillations in a coupled ocean–atmosphere model. *J. Atmos. Sci.,* **45,** 549–566.

Stephenson, D. B., 1997: Correlation of spatial climate/weather maps and the advantages of using the Mahalanobis Metric in predictions. *Tellus*, **49,** 513–527.

Thompson, C. J., 1998a: Initial conditions for optimal growth in a coupled ocean–atmosphere model of ENSO. *J. Atmos. Sci.,* **55,** 537–557.

——, 1998b: A linear, stochastic, dynamical model of El Niño/Southern Oscillation. Ph.D. thesis, University of Washington, 235 pp.

——, and D. S. Battisti, 2000: A linear stochastic dynamical model of ENSO. Part I: Model development. *J. Climate*, **13,** 2818–2832.

Torrence, C., and P. Webster, 1998: The annual cycle of persistence in the El Niño–Southern Oscillation. *Quart. J. Roy. Meteor. Soc.*, **124,** 1985–2004.

Walker, G. J., and E. W. Bliss, 1937: *World Weather IV*. Vol. 4. Mem. Royal Meteorological Society, 119–139.

Wallace, J. M., E. M. Rasmusson, T. P. Mitchell, V. E. Kousky, E. S. Sarachik, and H. von Storch, 1998: On the structure and evolution of ENSO-related climate variability in the tropical Pacific: Lessons from TOGA. *J. Geophys. Res.,* **103,** 14 241–14 259.

Weiss, J. P., and J. B. Weiss, 1999: Quantifying persistence in ENSO. *J. Atmos. Sci.,* **56,** 2737–2760.

Zebiak, S. E., and M. A. Cane, 1987: A model ENSO. *Mon. Wea. Rev.*, **115,** 2262–2278.

Zhang, Y., J. M. Wallace, and D. S. Battisti, 1997: ENSO-like interdecadal variability: 1900–93. *J. Climate*, **10,** 1004–1020.